

AWARD NUMBER:  
W81XWH-12-1-0076

TITLE:  
Development of Laser-Mediated Nanodroplet Real-Time PCR on Circulating Tumor Cells (CTC) by Microfilter Platform

PRINCIPAL INVESTIGATOR:  
Gregory W. Faris, Ph.D.

CONTRACTING ORGANIZATION:  
SRI International

Menlo Park, CA 94025

REPORT DATE:  
June 2015

TYPE OF REPORT:  
Final

PREPARED FOR: U.S. Army Medical Research and Materiel Command  
Fort Detrick, Maryland 21702-5012

DISTRIBUTION STATEMENT: Approved for Public Release;  
Distribution Unlimited

The views, opinions and/or findings contained in this report are those of the author(s) and should not be construed as an official Department of the Army position, policy or decision unless so designated by other documentation.

REPORT DOCUMENTATION PAGE				Form Approved OMB No. 0704-0188	
Public reporting burden for this collection of information is estimated to average 1 hour per response, including the time for reviewing instructions, searching existing data sources, gathering and maintaining the data needed, and completing and reviewing this collection of information. Send comments regarding this burden estimate or any other aspect of this collection of information, including suggestions for reducing this burden to Department of Defense, Washington Headquarters Services, Directorate for Information Operations and Reports (0704-0188), 1215 Jefferson Davis Highway, Suite 1204, Arlington, VA 22202-4302. Respondents should be aware that notwithstanding any other provision of law, no person shall be subject to any penalty for failing to comply with a collection of information if it does not display a currently valid OMB control number. <b>PLEASE DO NOT RETURN YOUR FORM TO THE ABOVE ADDRESS.</b>					
1. REPORT DATE 1 June 2015		2. REPORT TYPE Final		3. DATES COVERED 15 Sept 2012- 14 March 2015	
4. TITLE AND SUBTITLE  Development of Laser-Mediated Nanodroplet Real-Time PCR on Circulating Tumor Cells (CTC) by Microfilter Platform				5a. CONTRACT NUMBER	
				5b. GRANT NUMBER W81XWH-12-1-0076	
				5c. PROGRAM ELEMENT NUMBER	
6. AUTHOR(S)  Gregory W. Faris, Ph.D.				5d. PROJECT NUMBER	
				5e. TASK NUMBER	
				5f. WORK UNIT NUMBER	
7. PERFORMING ORGANIZATION NAME(S) AND ADDRESS(ES) SRI International 333 Ravenswood Avenue Menlo Park, CA 94025-3493				8. PERFORMING ORGANIZATION REPORT NUMBER	
9. SPONSORING / MONITORING AGENCY NAME(S) AND ADDRESS(ES)  U.S. Army Medical Research and Materiel Command Fort Detrick, Maryland 21702-5012				10. SPONSOR/MONITOR'S ACRONYM(S)	
				11. SPONSOR/MONITOR'S REPORT NUMBER(S)	
12. DISTRIBUTION / AVAILABILITY STATEMENT  Approved for Public Release; Distribution Unlimited					
13. SUPPLEMENTARY NOTES					
14. ABSTRACT This project concerns analysis of circulating tumor cells (CTCs), which are proving to be important for prognostics and guiding therapy for breast cancer patients. The project is a collaboration between the University of Miami on the use of microfilters for capture of circulating tumor cells and SRI International on the use of nanodroplet real-time polymerase chain reaction (PCR) for molecular analysis of captured cells. To improve the temperature control for droplet PCR on the University of Miami microfilters, we have extended our DNA melting temperature calibration methodology to use DNA hairpins and dyes that are less sensitive to temperature, adapted our melting and fitting model for the hairpins, have switched the laser heating from a wavelength of 1.45 to 1.9 $\mu\text{m}$ , performed sensitivity studies on the influence of water and glycerol on the calibration, and developed software for real-time same-droplet temperature calibration as an image across the droplet. Together with the University of Miami we have produced a strategy for spectrally-multiplexed Taqman to analyze for hMAM, CEA, KRT19 and MUC1 gene expression, including multiplexing optics and relevant primers and probes. We have performed simultaneous multiplexed detection of the four genes using laser-heating PCR in nanoliter droplets at SRI from cDNA prepared at the University of Miami from breast cancer cell lines.					
15. SUBJECT TERMS Circulating tumor cells, breast cancer, polymerase chain reaction, microfilters					
16. SECURITY CLASSIFICATION OF:			17. LIMITATION OF ABSTRACT	18. NUMBER OF PAGES	19a. NAME OF RESPONSIBLE PERSON
a. REPORT	b. ABSTRACT	c. THIS PAGE			USAMRMC
Unclassified	Unclassified	Unclassified	Unclassified	34	19b. TELEPHONE NUMBER (include area code)

## TABLE OF CONTENTS

1. Introduction .....	4
2. Keywords.....	4
3. Overall Project Summary.....	4
4. Key Research Accomplishments.....	15
5. Conclusion .....	15
6. Publications, Abstracts, and Presentations .....	16
7. Inventions, Patents and Licenses .....	16
8. Reportable Outcomes .....	16
9. Other Achievements.....	17
10. References.....	17
11. Appendices .....	19

## INTRODUCTION

This project concerns analysis of circulating tumor cells (CTCs), which are proving to be important for prognostics and guiding therapy for breast cancer patients.<sup>1-8</sup> The project, a collaboration between the University of Miami on the use of microfilters for capture of circulating tumor cells and SRI International on the use of nanodroplet real-time polymerase chain reaction (PCR) for molecular analysis of captured cells. This report describes work performed at SRI to combine these two methods for analysis of CTCs. This builds on prior work that uses a laser for manipulation and processing of nanoliter droplets.<sup>9-15</sup>

## KEYWORDS

Circulating tumor cells, breast cancer, polymerase chain reaction, microfilters.

## OVERALL PROJECT SUMMARY

### **Task 1: Capture of CTC using microfilter device for immunofluorescence identification and on-filter nanodroplet laser-heated real-time PCR.**

Zheng Ao of the University of Miami (graduate student under Prof. Ram Datar) and Drs. Gregory Faris and Eric Hall met at SRI to test the use of the laser-heating PCR on the microfilters. Assessment of the filters for CTC capture and immunofluorescence identification resulted in the conclusion that achieving droplet stability on the filters would require significant fine tuning of the matrix oil properties. A lecithin concentration of 0.08% (v/v) in a mineral oil matrix was required to eliminate erratic droplet movement on the filter to allow for precise droplet spotting.

Figure 1 summarizes our preliminary data on the effect of lecithin concentration on droplet stability on three different substrates: polystyrene (petri dish), parylene HT, and porous parylene HT (filter). It demonstrates that, as lecithin concentration increases, a droplet can become more unstable. Interestingly, while there does not appear to be a significant difference between polystyrene and non-porous parylene HT, the instability caused by lecithin is enhanced on porous parylene HT. In fact, at 1% lecithin, 5 out of 6 droplets in a set lose sufficient cohesion that they spread out beyond the camera's field of view. The area determination of droplets that exhibited this behavior was less reliable, so they were not included in the data and instead denoted by parenthetical numbers above the relevant bars in Figure 1. Droplets on various surfaces including the microfilter are shown in Figure 2.

The ability to produce small drops was another technical milestone that was accomplished in this study. Filter based or droplet based single cell lysis, downstream PCR, and four probe multiplexing using an optical microscope required average droplet sizes of 100-120  $\mu\text{m}$ . By adjusting the parameters for our automated droplet generation system we can now make droplets with diameters of 50 microns routinely.

We have developed automated ImageJ-based routines for identification of CTCs based on labeling and morphology. These can run in a batch mode to identify likely CTCs.

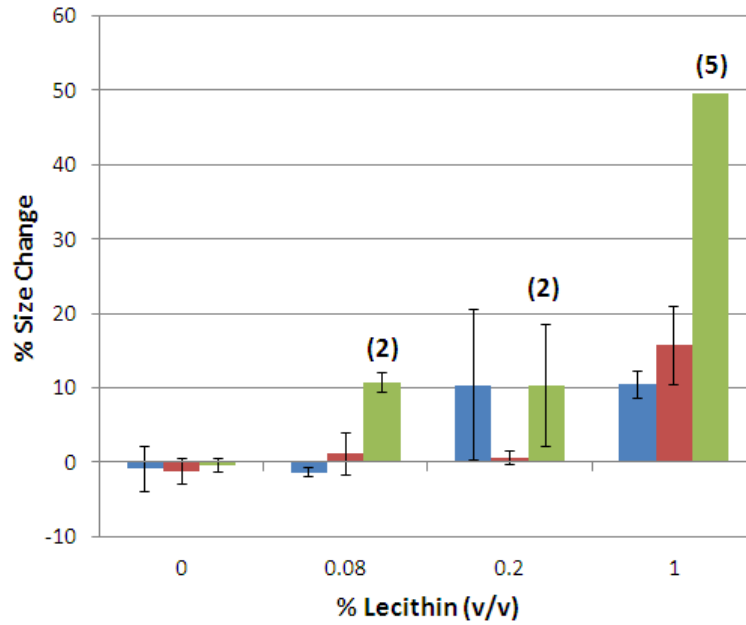
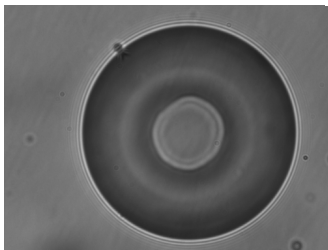
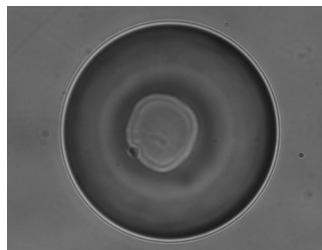


**Figure 1.** Change in droplet stability (size) on different substrates as a function of lecithin concentration in the oil phase. Substrates are polystyrene (blue), parylene HT (red) and porous parylene HT (green). Parenthetical numbers above a given bar indicate the number of droplets in a set of six whose size could not be measured due to sufficient loss of cohesion that they spread out over an area greater than the camera's field of view.

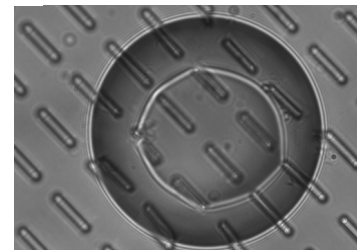
### Hydrophobic surfaces



0.08% lecithin,  
polystyrene

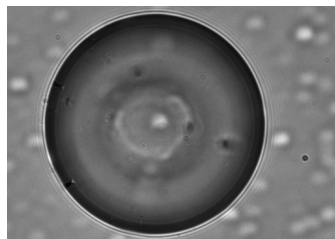


No lecithin, parylene



No lecithin, filter

### Hydrophilic surfaces



1.3% lecithin, glass slide

**Figure 2.** Droplets dispensed onto different surfaces.

## **Task 2: Viable cell capture and immunofluorescence for identification of CTC to be analyzed off-filter by nanodroplet laser-heated real-time PCR.**

To date we have performed immunofluorescence imaging of cancer cell lines at SRI. Imaging has been performed using conventional fluorescence filters sets, the dye DAPI as a nuclear stain, and labels for cytokeratin and CD45. Data for cDNA analysis in droplets is provided in Task 3.

## **Task 3: Optical microfluidics to perform immunofluorescence and nanodroplet laser-heated real-time PCR.**

To date, we have been primarily using disposable polystyrene Petri dishes for our substrates. We found that working with different substrate types such as the parylene microfilters leads to significant changes in the droplet heating even when using the same laser intensity. This is largely due to changes in the droplet shape, although substrate transparency, reflections, and distortions also can play a role. Our preliminary efforts to stabilize droplet geometry are discussed above in Task 1.

### **(1) In-Droplet Temperature Calibration:**

Accurate and reliable PCR requires consistent heating of droplets by our infrared laser. However, changes in the interaction of the infrared laser with the droplet can alter heating behavior, thus changing the thermocycling protocol and hindering reliability and reproducibility. To provide accurate thermometry for infrared laser-assisted heating in microdroplet PCR,<sup>16-18</sup> we have developed a temperature calibration method that relies on the melting of contact-quenched fluorescently labeled DNA oligomers. An oligomer labeled with a 5' fluorescent reporter is contact-quenched by a 3' quencher on the reverse complement upon hybridization.<sup>19-22</sup> Upon heating and dissociation of the hybrid pair, the fluorescence of the reporter oligomer is detected and recorded. The melting points of several oligomer pairs are assigned with a traditional qPCR instrument and used to calibrate temperature in the microdroplet with laser heating when this process is repeated at the microscale. This method not only provides a reliable and consistent calibration for microdroplet heating, as demonstrated by proper selection of heating parameters for qPCR, but it is also simple and straightforward to perform. Although we use this method for system calibration, it can be applied to online temperature monitoring during PCR while consuming only a single fluorescence channel as described further below. A published paper more fully describing this work may be found in the Appendix. This work used hybridization of two oligos as the melting calibration and requires excess quenching oligo for accurate results and may be subject to systematic errors in kinetics and hybridization that can influence the temperature calibration. To minimize these effects and to adapt this method for in-droplet temperature calibration to perform PCR in droplets, two temperature probe hairpins were designed to allow for simultaneous use with cDNA from cell lines of interest and primers and probes to achieve qPCR in droplets for detecting specific gene expression in the chosen cell lines. These hairpin-based probes have fluorophore and quencher that are less temperature dependent and less subject to contact quenching. The sequences for the hairpins are shown in Table 1. These probes have melting temperatures of 64.5 and 83.5 °C for a Taqman master mix and 57 and 79 °C for the Kapa master mix.

Table 1. Hairpin sequences for temperature calibration inside droplets

Name	Manufacturer	Sequence
Low Hairpin	IDT	CGATATAATTTTTTTTTTTTTTTTTTTTTTTTTTTTAATTATATCG
High Hairpin	IDT	CGACAAGAGGGTCGTTTTTTTTTTTTTTTTTTTTTCGACCCTCTTGTCG

The high hairpin probe is a 76 basepair sequence that does not interfere with qPCR signals for gene expression of the selected genes. It has a melt temperature of around 83 °C and is well suited to characterize laser voltages that would enable droplet heating to 95 °C and around 60 °C for the PCR reaction. The high hairpin probe provides a robust droplet temperature calibration and a one-time single calibration in the chosen PCR master-mix is required to get accurate melt temperatures using a benchtop instrument such as the LightCycler 480 (Roche). As an example, temperature variations within a 115  $\mu\text{m}$  droplet are shown in Figure 3 below and are less than 6 degrees Celsius when a thermal melt is performed with the high melt DNA hairpin.

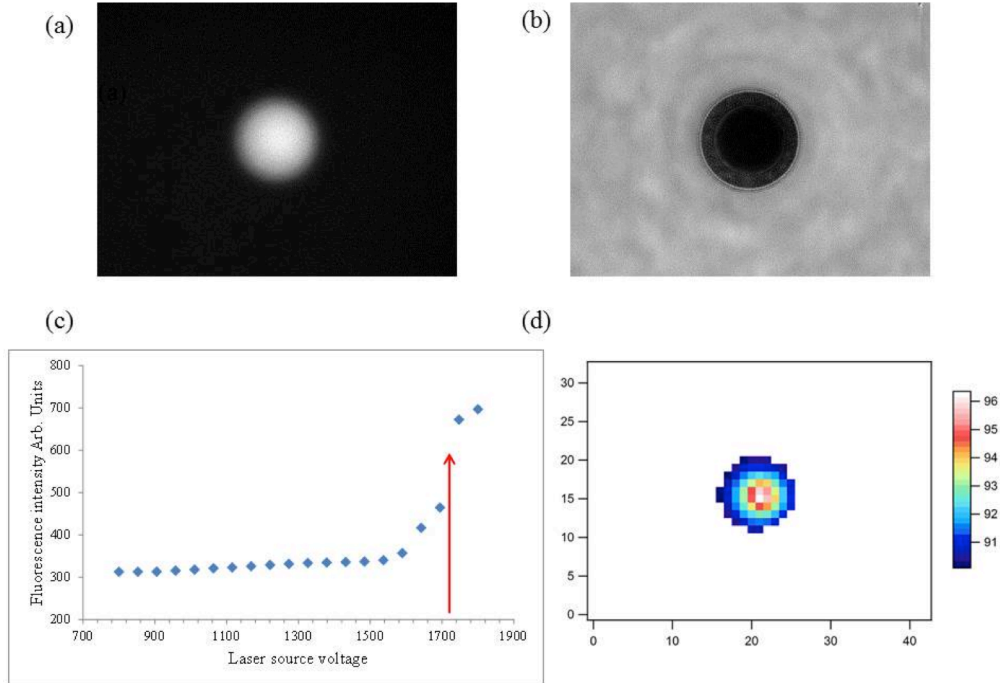


**Figure 3:** (a) Fluorescence profile of a 115  $\mu\text{m}$  aqueous droplet containing a DNA hairpin in a PCR master mix solution as measured using the ROX channel of the spectral filter cube at a voltage of 1694 mV. (b) The corresponding brightfield image showing the laser footprint in the drop as a shadow graph. (c) The integrated intensity from the droplet in (a) as a function of increasing laser voltage (mV), i.e. corresponding to an increasing temperature. The melt profile of the DNA hairpin is clearly seen. (d) Measured temperature calibration inside the droplet using a model developed by Hall and Faris. The melting of the hairpin was used to measure the temperature profile of the droplet when a 1.9 micron laser beam is used to heat the droplet. The measured  $T_m$  of this hairpin is 83 °C. The temperature scale bar indicates a variation of only 6 degrees Celsius across the droplet. These data were taken with the microscope in the emission multiplexing mode.

## (2) Microscopy Platform and Multiplexed PCR with cDNA Amplicons:

Working with the University of Miami, we have developed a strategy for measurement of the four gene targets: hMAM, CEA, KRT19, and MUC1 from cell the following cell lines: SKBR3, MCF-7 and MDA-MB-468. Each gene target is labeled with a unique probe and the design included a Taqman detection scheme for PCR. The University of Miami has designed primer and probe sequences for simultaneous PCR to analyze for hMAM, CEA, KRT19 and MUC1 gene expression. The primer and probe sequences are listed in Table 2.

Table 2. Primer pair and probe sequences for hMAM, CEA, KRT19 and MUC1

Target	Forward Primer	Length	Reverse Primer	Length	Probe	Length
hMAM	CAAGACCTTTGG CTCACAGAAC	22	GAAGGTGTGGTT TGCAGCAATC	22	TGCAGGGTATGGTG AGAAACCAACTA	26
CEA	GGCTACTGGCCG CAATAATTC	21	CCAACCAGCACT CCAATCATG	21	AGTCAAGAGCATCA CAGTCTCTGCATC	27
KRT19	CGCCAAGATCCT GAGTGACAT	21	CGACCTCCCGGT TCAATTCTTC	22	CCAATATGAGGTCA TGGCCGAGCA	24
MUC1	CGCTGGCCATTG TCTATCTCATTG	24	ATCCCGGGCTGG AAAGATG	19	CTGTCTGTCAGTGC CGCCGAA	21

Our first optical design included a quad band filter set that included an excitation filter 89101x, beam splitter 89100bs and emission filter 89101m from Chroma and was coupled to an emission multiplexing scheme where an emission filter wheel present before the camera on the imaging microscope would allow probe specific signals for droplet imaging during real time PCR. The additional emission filter 89101m was needed to block leakage between the excitation and individual emission filters, which otherwise presents a background. This optical design is labeled as *emission based multiplexing*. Individual excitation filters for each channel are listed in Table 3 for each of the targets hMAM, CEA, KRT19, and MUC1. Multiplexed Taqman assays are used to support four spectral channels.

Table 3. Spectral channels for emission based multiplexed PCR.

Target	Probe Label	Dye Excitation (nm)	Dye Emission (nm)	Emission Filter
hMAM	Pacific Blue	416	451	ET 455/50m
CEA	FAM	494	525	ET 525/36m
KRT19	Rhodamine Red-X	560	580	ET 605/52m
MUC1	Cy5	646	667	ET 705/72m

To enable experiments with the new quadband filter sets mentioned above, measurements were also performed to record the transmitted laser power of the 1.46  $\mu\text{m}$  laser through the quadband dichroic. A significant loss of laser power was noted. To address this issue, a 1.9  $\mu\text{m}$  laser was integrated into the microscope set up to enable droplet heating. Using modifications made to the droplet dispensing apparatus and using squalane as the oil matrix to maintain



consistency in the oil matrix composition (mineral oil as an oil matrix posed potential issues with lot to lot variability in composition), deposition of droplets in the 50-120  $\mu\text{m}$  size range is now routinely achieved. Examples of droplet heating parameters with the high hairpin probe are shown in Figure 4.

The ability to perform same droplet temperature calibration may be affected by the fact that some PCR reagents may contain small quantities of glycerol. Dilution by water or glycerol does have a significant effect on the melting temperature of the DNA hairpin and hence droplet temperature calibration for PCR runs. Dilution by either water or glycerol reduces the melting temperature, with the glycerol having a larger impact than water. Heating for droplet temperature calibration and for subsequent PCR in the droplet both result in some loss of the aqueous environment to the oil matrix. If the droplets lose significant amounts of either water or glycerol during heating, this would lead to a higher melting temperature. The melting temperature decreases by about 7 degrees for a 50% dilution by water. If this slope remains constant for loss of water, a droplet area reduction of 20% (around 30% in volume) would lead to an increase in melting temperature of roughly 5 degrees. These observations further support the need to have accurate in droplet temperature calibration for reliable PCR and a first melt temperature calculation using a bench top instrument for a specific PCR master mix that includes all the components of the reaction mixture.

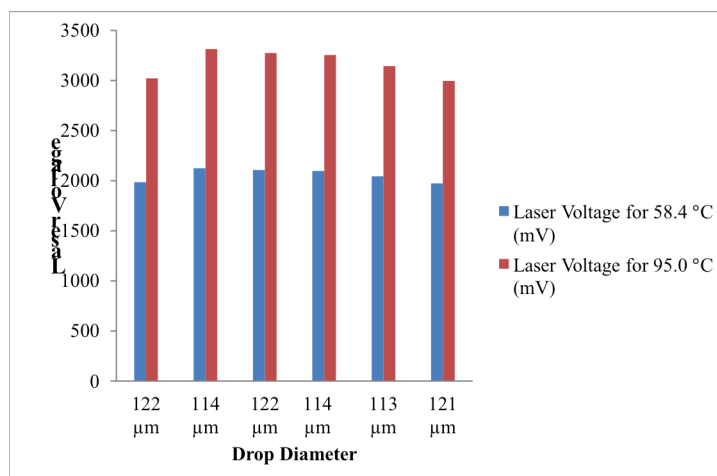


**Figure 4.** Laser voltages measured via calibration using the high hairpin in each drop prior to performing PCR. The drops are of comparable sizes and the laser voltages calculated from fitting the hairpin melt curve are for the annealing and extension temperature of 58.4 °C and denaturation temperature of 95 °C.

To test the optical design (emission multiplexing) amplicons were made from the cDNA of the SKBR3 cell lines supplied by the Datar lab at the University of Miami and used as templates in preliminary system design and testing. These amplicons were not purified prior to use. Amplicons were used to save time on instrument design troubleshooting. Preliminary duplexing experiments using the Pacific Blue and FAM probes for the hMAM and CEA targets resulted in very good PCR signal. Amplicons for each target were diluted by a factor of  $10^4$  from the original stock and data from these runs is shown in Figures 4 and 5. A master sample was made using 20  $\mu\text{L}$  of the Fast Universal Master Mix from Life technologies (2X), 0.5  $\mu\text{L}$  of BSA (50 mg/ml stock solution), 1  $\mu\text{L}$  Platinum Taq polymerase (Life Technologies), high hairpin (0.375  $\mu\text{M}$ ), and probes (1  $\mu\text{M}$  hMAM, 0.5  $\mu\text{M}$  CEA), primers (10  $\mu\text{M}$ ) and amplicons for the hMAM and CEA genes. Amplification curves were obtained from both gene targets with Ct values comparable to corresponding singleplex runs with each target amplicon (data not shown). As

noted in Table 4, annealing and extension times of as low as 10 seconds and an initial hot-start and denaturation time of as little as 10 seconds resulted in PCR amplification with high primer concentrations in the droplets.

Table 4. PCR cycling parameters for data in Figure 5.

Drop number, Drop diameter ( $\mu\text{m}$ )	First denaturation and hot-start (sec.)	Wait time (sec.)	PCR annealing and extension (sec.)	PCR denaturation (sec.)
1, 122	20	10	20	1
2, 114	20	10	20	1
3, 122	20	10	10	1
4, 114	20	10	10	1
5, 113	20	10	5	1
6, 121	10	1	20	1

Our next attempt to multiplex 3 or 4 target amplicon templates (hMAM, CEA, KRT19, and MUC1) in droplet PCR at a  $10^2$  or  $10^4$  dilution from the original stock resulted in photo-bleaching of the hMAM probe and weak amplification of the CEA amplicons and weak signals for the MUC1 probe. On testing the transmission properties of the 1.96 micron laser dichroic, we observed dips in the spectral channel for the Cy5 (MUC1 Probe) emission wavelengths. We decided to modify the apparatus and tested an ITO (Indium Tin Oxide) coated dichroic to reflect the 1.96 micron laser beam into the microscope objective. ITO was chosen due to its high transparency in the visible spectral region and high reflectance in the far infrared region. This helped reduce the exposure times for the Cy5 channel considerably to allow for multiplexing of 3 target amplicons. However, we still had photo bleaching at higher cycles from the Pacific Blue channel. The mercury lamp light source on our microscope platform also proved to be inadequate for efficient excitation of the Cy5 probe due to a large dip in the emission in the 600 nm wavelength range for this light source. In Figure 6(a), multiplexing results from hMAM, CEA and MUC1 amplicon targets ( $10^4$  dilution, probes at 0.5  $\mu\text{M}$ , high hairpin at 0.4  $\mu\text{M}$ , primers at 10  $\mu\text{M}$ , 1X Taqman Fast Universal master mix, 1 ul Platinum Taq Polymerase, and 0.5  $\mu\text{L}$  of BSA from a 50 mg/mL stock solution combined in a 40  $\mu\text{L}$  volume) are shown with the mercury light source and an ITO coated dichroic. Photo

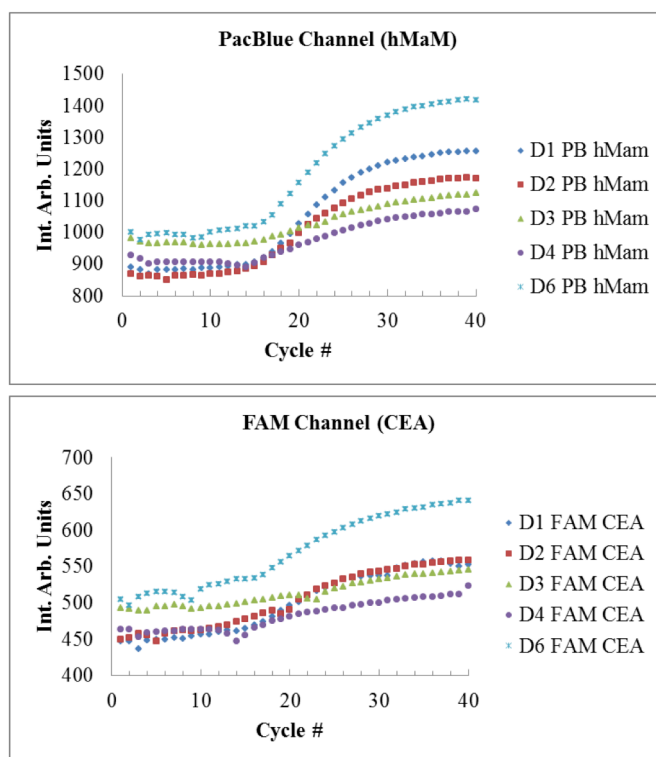


**Figure 5.** Duplex real time PCR signals from hMAM and CEA amplicons in droplets shown in Figure 4. PCR cycling parameters are shown in Table 4.

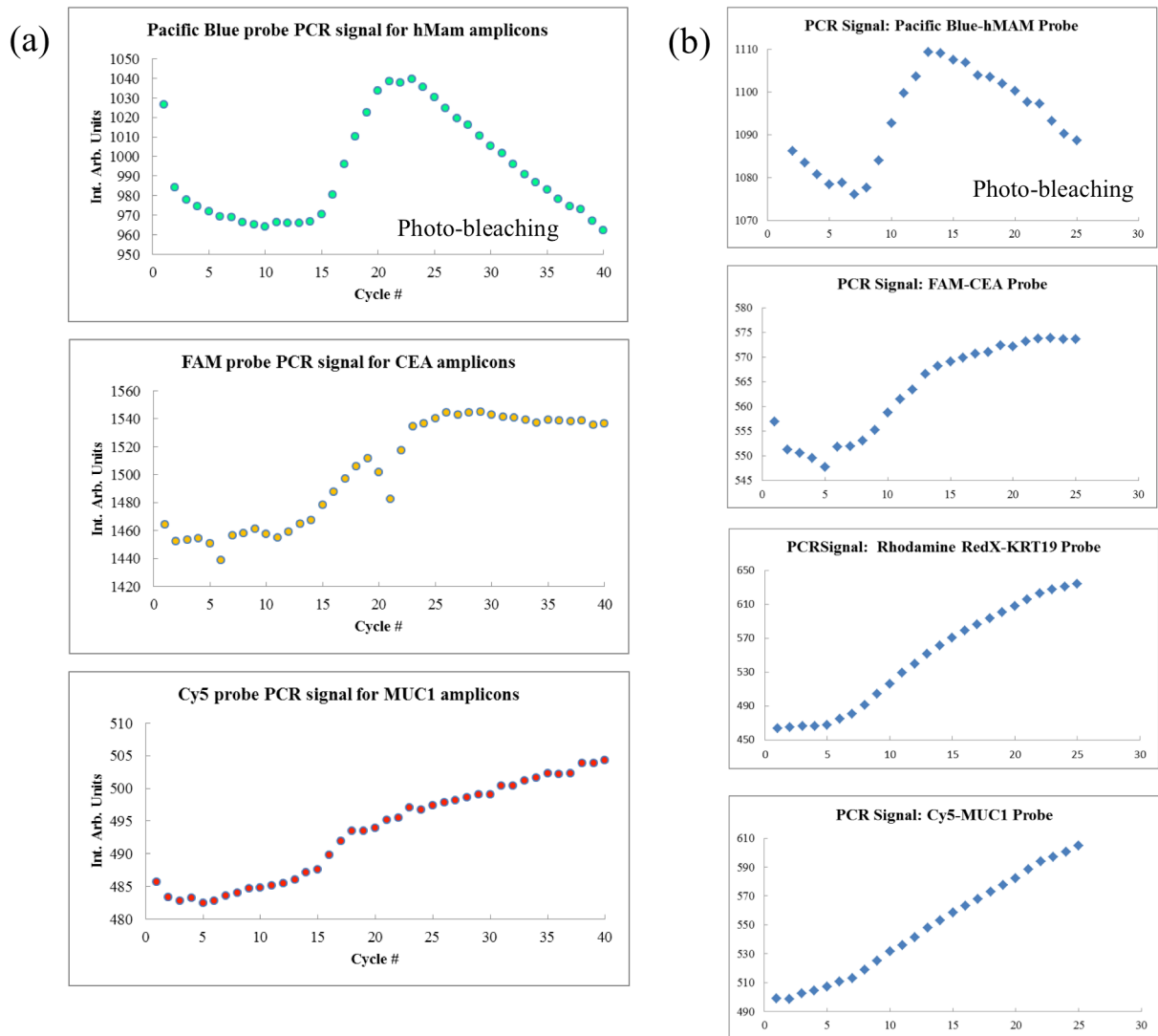


**Figure 6.** Raw multiplexed PCR data from 1 nL droplets: (a) Three target multiplexing with templates (hMAM, CEA, MUC1) in droplet PCR at  $10^4$  dilution from the original stock, (b) Four target multiplexing with templates (hMAM, CEA, KRT19, MUC1) in droplet PCR at  $10^2$  dilution from the original stock. Note the shift in Ct to lower values when a higher concentration of amplicons is used. Raw Intensity is plotted on the Y axis, Cycle # is plotted on the X axis.

bleaching from the Pacific Blue probe is observed after cycle 20. Also observed is the onset of photo bleaching from the FAM probe and very low signal to noise ratio in the signals from the Cy5 probe. The mercury light source has several emission peaks, with strong signals at 405, 436, 546 and 579 nm. The increased photo bleaching of the Pacific Blue probe is can be attributed to signal from the light source exciting the probe for every exposure due to the emission based multiplexing design of the experiment. Experiments performed with single channel exposure with the Pacific Blue channel resulted in no photo bleaching of the dye. Four probe-based multiplexing using target amplicon templates at a  $10^2$  dilution from the stock, 0.25  $\mu$ M probes for hMAM, CEA and KRT19, 5  $\mu$ M probe for MUC1, 5  $\mu$ M primers, 0.375  $\mu$ M high hairpin probe, 1X Taqman Fast Universal master mix, 1 ul Platinum Taq Polymerase, and 0.5  $\mu$ L of BSA from

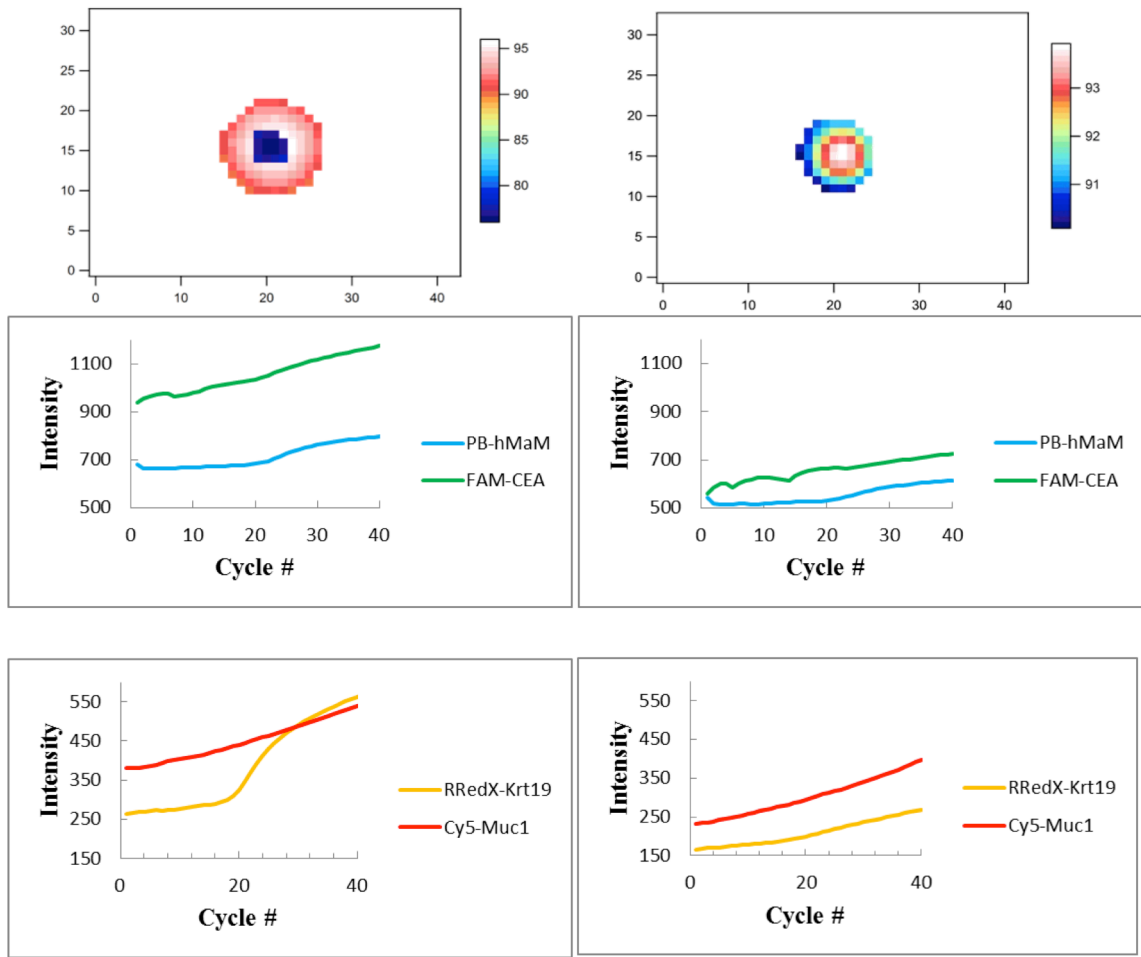
a 50 mg/mL stock solution combined in a 40  $\mu$ L volume, resulted in successful multiplexed PCR signals from all four probes but with accompanied photo bleaching as shown in Figure 6(b). Based on these results, the imaging platform was redesigned to enable excitation-based multiplexing which would select narrow wavelength channels to excite multiple probes in the droplets to allow for multiplexing and minimize photo bleaching. Excitation filters specific to each probe were ordered or used from in-house optical components, the details of which are given in Table 5. Also purchased new was a dichroic specifically designed for fluorescence microscopy that was coated with ITO.

Table 5. Spectral channels for excitation based multiplex PCR.

Target	Probe Label	Dye Excitation (nm)	Dye Emission (nm)	Emission Filter
hMAM	Pacific Blue	416	451	EX 405/30x
CEA	FAM	494	525	EX 480/40x
KRT19	Rhodamine Red-X	560	580	EX 560/40x
MUC1	Cy5	646	667	EX 620/60x

In order to perform excitation based multiplexing, preliminary control experiments were performed after installing a Xenon lamp in our system to allow for uniform illumination of all four probes. Amplicons were diluted to  $10^5$  for the hMAM, CEA and MUC1 target genes and about  $10^4$  for the KRT19 target gene. A single large aspirated drop (140  $\mu$ m) resulted in signals from all four probes with the strongest signal to noise for the KRT19 amplicons. However, when the same solution was used the next day (from frozen, the polymerase is a hot-start enzyme, freezing prepared PCR samples appears to not affect the reaction for up to several days when in the freezer), only 2 in 4 droplets showed amplification of at least one target amplicons, the drop sizes were smaller though, by almost 50% and were in the 100  $\mu$ m diameter specification. Data from these runs are shown in Figure 7.

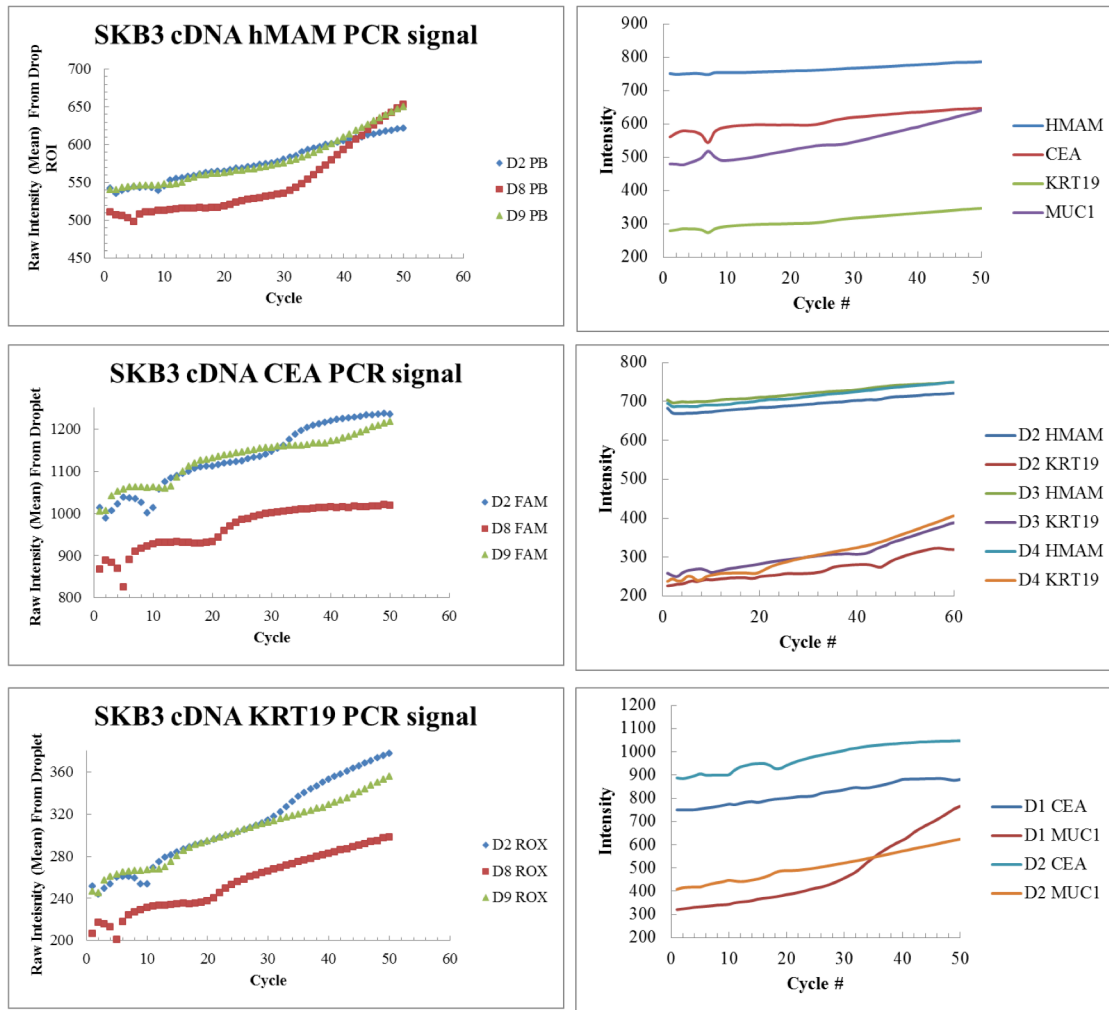
To perform excitation multiplexing with cDNA directly from lysed cells, we next attempted to perform in-droplet PCR from cDNA reverse transcribed from cells (SKBR3, MCF7 and MDA-MD-468) by our collaborators in Miami. While performing control experiments during this phase of the study, contamination of reagents was found to have occurred during prior test with the amplicons. New reagents (primers, probes, Platinum TAQ polymerase) were immediately ordered. All new reagents were tested for PCR using the Roche Light Cycler 480 instrument. In our early experiments with cDNA, it was noted that successful amplification of all four cDNA fragments of interest were not observed in droplet experiments. These data are shown in Figure 8. This is to be expected because the cDNA was present at less than single cellular concentrations. For experiments with cDNA production through in-droplet lysis we expect to achieve better results.



Drop diameter = 140  $\mu\text{m}$

Drop diameter = 102  $\mu\text{m}$

**Figure 7.** Excitation multiplexing based PCR data from two drops containing 4 different amplicons target genes. Weak amplification is observed for the CEA and MUC1 amplicon targets but detectable signal is observed for the hMaM and KRT19 amplicon targets. Both drops had the same sample, and similar exposure times. The PCR solution included BSA, Platinum TAQ DNA polymerase and high hairpin for in droplet temperature calibration.



(a) SKBR3 cDNA – triplex runs in droplets

(b) SKBR3 cDNA – fourplex and duplex runs in droplets

**Figure 8.** Excitation multiplexing based droplet PCR for cDNA from SKBR3 cell lines. cDNA was formed via reverse transcription and added to the PCR mix without further purification. Panel (a) shows data from triplex experiments where the hMAM, CEA and KRT19 genes were amplified. Panel (b) shows data from fourplex and duplex experiments with hMAM, CEA, KRT19 and MUC1 genes. In all experiments, primer concentration and polymerase concentrations were varied to explore the parameter space of variables.

#### Task 4: Integration of the CTC microfilter capture and nanodroplet laser-heated real-time PCR platforms into a single device.

As described in Task 1, we have developed a temperature calibration method to allow compensation for variations in droplet size, shape, and contact angle when using irregular surfaces such as the microfilters. These steps provide the basis for integration of the microfilter and laser PCR technologies because of the influence of the microfilter slots on the droplet size, shape, and contact angle. Analysis of cDNA prepared at the University of Miami using laser heating PCR in nanoliter droplets is described under Task 3.

## KEY RESEARCH ACCOMPLISHMENTS

- We have developed a temperature calibration method based on DNA melting to improve temperature accuracy for droplet PCR.
- We have developed a model that incorporates fluorescence pre-melting to support the temperature calibration described above.
- We have improved our ability to produce small droplets in the range of 50 microns.
- We have assessed the instability of droplet geometry on the capture filters using our current lecithin-based protocol and are now identifying candidates for improvement.
- We have extended the temperature calibration method to use hairpin oligos instead of an oligo pair and use dyes with lower temperature sensitivity.
- We have developed software for online calibration of temperature in each droplet.
- We have performed calibrated heating in droplets down to 100 microns.
- We have confirmed performance of the Taqman probes developed by the University of Miami.
- PCR via multiplexing in droplets using amplicons and cDNA has been demonstrated.

## CONCLUSION

This project concerns analysis of circulating tumor cells (CTCs), which are proving to be important for prognostics and guiding therapy for breast cancer patients. The project, a collaboration between the University of Miami on the use of microfilters for capture of circulating tumor cells and SRI International on the use of nanodroplet real-time polymerase chain reaction (PCR) for molecular analysis of captured cells. To improve the temperature control for droplet PCR on the University of Miami microfilters, we have extended our DNA melting temperature calibration methodology to use DNA hairpins and dyes that are less sensitive to temperature, adapted our melting and fitting model for the hairpins, have switched the laser heating from a wavelength of 1.45 to 1.9  $\mu\text{m}$ , performed sensitivity studies on the influence of water and glycerol on the calibration, and developed software for real-time same-droplet temperature calibration as an image across the droplet. Together with the University of Miami we have produced a strategy for spectrally-multiplexed Taqman to analyze for hMAM, CEA, KRT19 and MUC1 gene expression, including multiplexing optics and relevant primers and probes. These have been tested both at Miami and SRI. The culmination of the optical design resulted in an excitation based multiplexing platform using a Xenon lamp as an excitation source. PCR using all the four target genes from cDNA reverse transcribed from cells has been demonstrated though with a low efficiency (approximately 25%). This is due to sub-cellular populations of cDNA in the 1 nL droplets that are generated by the robotic platform. Current experiments are underway to increase cDNA yield and to get final sets of data for a publication.

## **PUBLICATIONS, ABSTRACTS, AND PRESENTATIONS**

### **Publication:**

- 1) Hall EW, Faris GW. Microdroplet temperature calibration via thermal dissociation of quenched DNA oligomers. *Biomed Opt Express*. 2014; 5(3):737-51. PMID: 3959839.

### **Manuscript:**

An manuscript that details results from the cDNA multiplexing experiments in droplet platforms is under preparation.

### **Presentations:**

1. Eric Hall and Gregory W. Faris, "Optical Control & Thermocycling Calibration of Laser-Heated Microdroplet PCR for Circulating Tumor Cell Analysis," (Invited) Presented at Molecular Med Tri-Con, San Francisco, California, February 9-14, 2014.
2. Eric W. Hall, Kanaka Hettiarachchi, Hanyoup Kim, and Gregory W. Faris, "Optical Control & Thermocycling Calibration of Laser-Heated Microdroplet PCR," Presented at Molecular Med Tri-Con, San Francisco, California, February 9-14, 2014.
3. Eric W. Hall and Gregory W. Faris, "Extraction Of Conventional Two-State Melting Temperature From DNA Oligomers With Significant Premelting Behavior," Paper PM 3513-Pos, Presented at Biophysical Society 58th Annual Meeting, San Francisco, California, February 15-19, 2014.
4. Eric W. Hall, Kanaka Hettiarachchi, Hanyoup Kim, Gregory W. Faris, "Optical Control of Microdroplets for Cell-Encapsulating Polymerase Chain Reaction," Paper BM2A.2, presented at Biomedical Optics (BIOMED), Miami, Florida, 26-30 April 2014.
5. Xiaohe Liu, Gregory Faris, Kanaka Hettiarachchi, George Solmo, Keith Laderoute and Lidia C. Sambucetti, "Methods for isolation and analysis of single circulating tumor cells (CTCs)," presented at Single Cell Analysis Investigators Meeting, Bethesda MD, April 15-16, 2013.
6. Gregory W. Faris, Sanhita Dixit, Eric Hall, Hanyoup Kim, and Kanaka Hettiarachchi, "Droplet microfluidics microscopy for cell analysis and artificial bilayers," presented at Advances in Optics for Biotechnology, Medicine and Surgery XIII, Granlibakken Hotel, Lake Tahoe, California, June 2-5, 2013.
7. Xiaohe Liu, Gregory Faris, Kanaka Hettiarachchi, George Solmo, Keith Laderoute and Lidia C. Sambucetti, "Methods for isolation and analysis of single circulating tumor cells (CTCs)," presented at Discover SRI: Biosciences Poster Day, International Building, SRI International, Menlo Park, CA, August 6, 2013.

## **INVENTIONS, PATENTS AND LICENSES**

None.

## **REPORTABLE OUTCOMES**

This research has advanced methods for performing PCR in droplets including development of temperature calibration methods, a model for fluorescence pre-melt, online droplet



temperature calibration, generation of small droplets, droplet instability, and strategies for wavelength multiplexed PCR.

## **OTHER ACHIEVEMENTS**

### **Employment and training:**

Two summer students supported by the Research Experiences for Undergraduates program sponsored by the National Science Foundation (Gary Wan, Gabriele Abraham) received training through participation in the research supported by this award. One postdoctoral fellow (Eric Hall) has received training through research on this project in this reporting period.

### **Personnel**

The following personnel received supported by this effort.

Dixit, Sanhita  
Faris, Gregory  
Graham, Jeanie  
Hall, Eric  
Kara, Laurie  
Liu, Xiaohe  
Olson, William  
Pan, Chia-Pin  
Wright, Jennifer  
Young, Steve

## **REFERENCES**

1. Onstenk W, Gratama JW, Foekens JA, Sleijfer S. Towards a personalized breast cancer treatment approach guided by circulating tumor cell (CTC) characteristics. *Cancer Treat Rev.* 2013; 39(7):691-700.
2. Gorges TM, Pantel K. Circulating tumor cells as therapy-related biomarkers in cancer patients. *Cancer Immunol Immunother.* 2013; 62(5):931-9.
3. Lianidou ES, Markou A, Strati A. Molecular characterization of circulating tumor cells in breast cancer: challenges and promises for individualized cancer treatment. *Cancer metastasis reviews.* 2012; 31(3-4):663-71.
4. Rack B, Bock C, Andergassen U, Doisneau-Sixou S. Hormone receptor status, erbB2 expression and cancer stem cell characteristics of circulating tumor cells in breast cancer patients. *Histol Histopathol.* 2012; 27(7):855-64.
5. Giordano A, Cristofanilli M. CTCs in metastatic breast cancer. *Recent Results Cancer Res.* 2012; 195:193-201.
6. Saloustros E, Mavroudis D. CTCs in primary breast cancer (II). *Recent Results Cancer Res.* 2012; 195:187-92.
7. Rack B, Andergassen U, Janni W, Neugebauer J. CTCs in primary breast cancer (I). *Recent Results Cancer Res.* 2012; 195:179-85.

8. Janni W, Rack B, Kasprowicz N, Scholz C, Hepp P. DTCs in breast cancer: clinical research and practice. *Recent Results Cancer Res.* 2012; 195:173-8.
9. Kotz KT, Gu Y, Faris GW. Optically addressed droplet-based protein assay. *J Am Chem Soc.* 2005; 127(16):5736-7.
10. Kotz KT, Noble KA, Faris GW. Optical microfluidics. *Appl Phys Lett.* 2004; 85(13):2658-60.
11. Dixit SS, Kim H, Vasilyev A, Eid A, Faris GW. Light-driven formation and rupture of droplet bilayers. *Langmuir.* 2010; 26(9):6193-200. PMID: 2896059.
12. Dixit SS, Pincus A, Guo B, Faris GW. Droplet shape analysis and permeability studies in droplet lipid bilayers. *Langmuir.* 2012; 28(19):7442-51.
13. Kim H, Dixit S, Green CJ, Faris GW. Nanodroplet real-time PCR system with laser assisted heating. *Opt Express.* 2009; 17(1):218-27. PMID: 3232056.
14. Kim H, Vishniakou S, Faris GW. Petri dish PCR: laser-heated reactions in nanoliter droplet arrays. *Lab Chip.* 2009; 9(9):1230-5. PMID: 3209801.
15. Hettiarachchi K, Kim H, Faris G. Optical manipulation and control of real-time PCR in cell encapsulating microdroplets by IR laser. *Microfluid Nanofluid.* 2012.
16. Hettiarachchi K, Kim H, Faris G. Optical manipulation and control of real-time PCR in cell encapsulating microdroplets by IR laser. *Microfluid Nanofluid.* 2012; 13(6):967-75.
17. Kim H, Dixit S, Green CJ, Faris GW. Nanodroplet real-time PCR system with laser assisted heating. *Opt Express.* 2009; 17(1):218-27.
18. Kim H, Vishniakou S, Faris GW. Petri dish PCR: laser-heated reactions in nanoliter droplet arrays. *Lab Chip.* 2009; 9(9):1230-5.
19. Marras SAE, Kramer FR, Tyagi S. Efficiencies of fluorescence resonance energy transfer and contact-mediated quenching in oligonucleotide probes. *Nucleic Acids Research.* 2002; 30(21):e122.
20. Johansson M. Choosing Reporter-Quencher Pairs for Efficient Quenching Through Formation of Intramolecular Dimers. In: Didenko V, editor. *Fluorescent Energy Transfer Nucleic Acid Probes*; Humana Press; 2006. p. 17-29.
21. Jung J, Chen L, Lee S, Kim S, Seong G, Choo J, et al. Fast and sensitive DNA analysis using changes in the FRET signals of molecular beacons in a PDMS microfluidic channel. *Anal Bioanal Chem.* 2007; 387(8):2609-15.
22. Jonstrup A, Fredsøe J, Andersen A. DNA Hairpins as Temperature Switches, Thermometers and Ionic Detectors. *Sensors.* 2013; 13(5):5937-44.
23. Hall EW, Faris GW. Microdroplet temperature calibration via thermal dissociation of quenched DNA oligomers. *Biomed Opt Express.* 2014; 5(3):737-51. PMID: 3959839.

## **APPENDICES**

**E. W. Hall and G. W. Faris, “Microdroplet temperature calibration via thermal dissociation of quenched DNA oligomers,” Biomed Opt Express 5, 737-751 (2014).**

# Microdroplet temperature calibration via thermal dissociation of quenched DNA oligomers

Eric W. Hall and Gregory W. Faris\*

Physical Sciences Division, SRI International, 333 Ravenswood Avenue, Menlo Park, CA 94025, USA

\*gregory.faris@sri.com

**Abstract:** The development of microscale analytical techniques has created an increasing demand for reliable and accurate heating at the microscale. Here, we present a novel method for calibrating the temperature of microdroplets using quenched, fluorescently labeled DNA oligomers. Upon melting, the 3' fluorophore of the reporter oligomer separates from the 5' quencher of its reverse complement, creating a fluorescent signal recorded as a melting curve. The melting temperature for a given oligomer is determined with a conventional quantitative polymerase chain reaction (qPCR) instrument and used to calibrate the temperature within a microdroplet, with identical buffer concentrations, heated with an infrared laser. Since significant premelt fluorescence prevents the use of a conventional (single-term) sigmoid or logistic function to describe the melting curve, we present a three-term sigmoid model that provides a very good match to the asymmetric fluorescence melting curve with premelting. Using mixtures of three oligomers of different lengths, we fit multiple three-term sigmoids to obtain precise comparison of the microscale and macroscale fluorescence melting curves using "extrapolated two-state" melting temperatures.

©2014 Optical Society of America

**OCIS codes:** (170.3890) Medical optics instrumentation; (170.2520) Fluorescence microscopy; (120.6780) Temperature.

## References and links

1. Y. T. Atalay, S. Vermeir, D. Witters, N. Vergauwe, B. Verbruggen, P. Verboven, B. M. Nicolai, and J. Lammertyn, "Microfluidic analytical systems for food analysis," *Trends Food Sci. Technol.* **22**(7), 386–404 (2011).
2. D. Wlodkowic and J. M. Cooper, "Tumors on chips: Oncology meets microfluidics," *Curr. Opin. Chem. Biol.* **14**(5), 556–567 (2010).
3. G. B. Salieb-Beugelaar, G. Simone, A. Arora, A. Philippi, and A. Manz, "Latest developments in microfluidic cell biology and analysis systems," *Anal. Chem.* **82**(12), 4848–4864 (2010).
4. S. Mondal and V. Venkataraman, "Novel fluorescence detection technique for non-contact temperature sensing in microchip PCR," *J. Biochem. Biophys. Methods* **70**(5), 773–777 (2007).
5. G. Velve Casquillas, C. Fu, M. Le Berre, J. Cramer, S. Meance, A. Plecis, D. Baigl, J.-J. Greffet, Y. Chen, M. Piel, and P. T. Tran, "Fast microfluidic temperature control for high resolution live cell imaging," *Lab Chip* **11**(3), 484–489 (2011).
6. C. Fang, L. Shao, Y. Zhao, J. Wang, and H. Wu, "A gold nanocrystal/poly(dimethylsiloxane) composite for plasmonic heating on microfluidic chips," *Adv. Mater.* **24**(1), 94–98 (2012).
7. K. J. Shaw, P. T. Docker, J. V. Yelland, C. E. Dyer, J. Greenman, G. M. Greenway, and S. J. Haswell, "Rapid PCR amplification using a microfluidic device with integrated microwave heating and air impingement cooling," *Lab Chip* **10**(13), 1725–1728 (2010).
8. B. Selva, J. Marchalot, and M.-C. Jullien, "An optimized resistor pattern for temperature gradient control in microfluidics," *J. Micromech. Microeng.* **19**(6), 065002 (2009).
9. H. Reinhardt, P. S. Dittrich, A. Manz, and J. Franzke, "micro-Hotplate enhanced optical heating by infrared light for single cell treatment," *Lab Chip* **7**(11), 1509–1514 (2007).
10. E. M. Graham, K. Iwai, S. Uchiyama, A. P. de Silva, S. W. Magennis, and A. C. Jones, "Quantitative mapping of aqueous microfluidic temperature with sub-degree resolution using fluorescence lifetime imaging microscopy," *Lab Chip* **10**(10), 1267–1273 (2010).

11. H. Kim, S. Dixit, C. J. Green, and G. W. Faris, "Nanodroplet real-time PCR system with laser assisted heating," *Opt. Express* **17**(1), 218–227 (2009).
12. H. Kim, S. Vishniakou, and G. W. Faris, "Petri dish PCR: Laser-heated reactions in nanoliter droplet arrays," *Lab Chip* **9**(9), 1230–1235 (2009).
13. K. Hettiarachchi, H. Kim, and G. Faris, "Optical manipulation and control of real-time PCR in cell encapsulating microdroplets by IR laser," *Microfluid. Nanofluid.* **13**(6), 967–975 (2012).
14. H. Terazono, A. Hattori, H. Takei, K. Takeda, and K. Yasuda, "Development of 1480 nm photothermal high-speed real-time polymerase chain reaction system for rapid nucleotide recognition," *Jpn. J. Appl. Phys.* **47**(6), 5212–5216 (2008).
15. R. P. Oda, M. A. Strausbauch, A. F. R. Hühmer, N. Borson, S. R. Jurens, J. Craighead, P. J. Wettstein, B. Eckloff, B. Kline, and J. P. Landers, "Infrared-mediated thermocycling for ultrafast polymerase chain reaction amplification of DNA," *Anal. Chem.* **70**(20), 4361–4368 (1998).
16. A. F. R. Hühmer and J. P. Landers, "Noncontact infrared-mediated thermocycling for effective polymerase chain reaction amplification of DNA in nanoliter volumes," *Anal. Chem.* **72**(21), 5507–5512 (2000).
17. J. Coppeta and C. Rogers, "Dual emission laser induced fluorescence for direct planar scalar behavior measurements," *Exp. Fluids* **25**(1), 1–15 (1998).
18. D. Ross, M. Gaitan, and L. E. Locascio, "Temperature measurement in microfluidic systems using a temperature-dependent fluorescent dye," *Anal. Chem.* **73**(17), 4117–4123 (2001).
19. M. A. Bennet, P. R. Richardson, J. Arlt, A. McCarthy, G. S. Buller, and A. C. Jones, "Optically trapped microsensors for microfluidic temperature measurement by fluorescence lifetime imaging microscopy," *Lab Chip* **11**(22), 3821–3828 (2011).
20. J. A. Richardson, T. Morgan, M. Andreou, and T. Brown, "Use of a large Stokes-shift fluorophore to increase the multiplexing capacity of a point-of-care DNA diagnostic device," *Analyst (Lond.)* **138**(13), 3626–3628 (2013).
21. S. A. E. Marras, F. R. Kramer, and S. Tyagi, "Efficiencies of fluorescence resonance energy transfer and contact-mediated quenching in oligonucleotide probes," *Nucleic Acids Res.* **30**(21), 122e (2002).
22. M. Johansson, "Choosing reporter-quencher pairs for efficient quenching through formation of intramolecular dimers," in *Fluorescent Energy Transfer Nucleic Acid Probes*, V. Didenko, ed. (Humana, 2006), pp. 17–29.
23. J. Jung, L. Chen, S. Lee, S. Kim, G. H. Seong, J. Choo, E. K. Lee, C.-H. Oh, and S. Lee, "Fast and sensitive DNA analysis using changes in the FRET signals of molecular beacons in a PDMS microfluidic channel," *Anal. Bioanal. Chem.* **387**(8), 2609–2615 (2007).
24. A. T. Jonstrup, J. Fredsøe, and A. H. Andersen, "DNA hairpins as temperature switches, thermometers and ionic detectors," *Sensors (Basel)* **13**(5), 5937–5944 (2013).
25. Y. You, A. V. Tataurov, and R. Owczarzy, "Measuring thermodynamic details of DNA hybridization using fluorescence," *Biopolymers* **95**(7), 472–486 (2011).
26. J.-L. Mergny and L. Lacroix, "Analysis of thermal melting curves," *Oligonucleotides* **13**(6), 515–537 (2003).
27. M. Peyrard, S. Cuesta-López, and G. James, "Nonlinear analysis of the dynamics of DNA breathing," *J. Biol. Phys.* **35**(1), 73–89 (2009).
28. F. J. Richards, "A flexible growth function for empirical use," *J. Exp. Bot.* **10**(2), 290–301 (1959).
29. J. H. Ricketts and G. A. Head, "A five-parameter logistic equation for investigating asymmetry of curvature in baroreflex studies," *Am. J. Physiol.* **277**, R441–R454 (1999).
30. J. SantaLucia, Jr., "A unified view of polymer, dumbbell, and oligonucleotide DNA nearest-neighbor thermodynamics," *Proc. Natl. Acad. Sci. U.S.A.* **95**(4), 1460–1465 (1998).
31. L. Movileanu, J. M. Benevides, and G. J. Thomas, Jr., "Temperature dependence of the Raman spectrum of DNA. II. Raman signatures of premelting and melting transitions of poly(dA).poly(dT) and comparison with poly(dA-dT).poly(dA-dT)," *Biopolymers* **63**(3), 181–194 (2002).
32. J. Jung and A. Van Orden, "A three-state mechanism for DNA hairpin folding characterized by multiparameter fluorescence fluctuation spectroscopy," *J. Am. Chem. Soc.* **128**(4), 1240–1249 (2006).

## 1. Introduction

The advent of microscale analytical technologies promises new advances in detection and quantitation in a variety of fields, from medicine to environmental monitoring to food safety [1–3]. However, as greater reproducibility and sensitivity are required for commercialization, there is a greater demand for more accurate and efficient methods of temperature control. Fulfilling this need is a non-trivial task, as many traditional techniques are incompatible with the confined spatial requirements of microfluidics [4, 5].

The wide variety of temperature control solutions that have been described in the literature can generally be sorted into contact and non-contact methods, though hybrid solutions also exist [6, 7]. Contact heating methods typically rely on resistive Joule heating or other solid-state elements to provide heating combined with thermometry feedback control. However, these are typically limited to integrated "lab-on-a-chip" microfluidic technologies,

where the critical elements are integrated into the chip architecture [6, 8–10]. For larger or more flexible systems in which the sample or reaction vessel is not limited to a pre-defined microscale area, this becomes prohibitively expensive or simply incompatible. Non-contact optical methods of temperature control are inherently more flexible and rely on radiation for heat delivery [7, 11–16].

A critical aspect of temperature control is temperature measurement for system calibration or feedback. Temperature-sensitive fluorescent dyes are one of the more popular methods of thermometry and are compatible with both contact and non-contact heating methods. Fluorescence methods, including both single-dye and ratiometric methods [4, 11, 12, 17–19], generally require calibration in the microscale system to compensate for temperature-dependent fluorescence efficiency and system-dependent spectral response. Such calibration is difficult because of the lack of practical temperature reference measurements at the microscale. Furthermore, ratiometric methods require measurement of multiple fluorescence wavelengths, reducing the throughput of spectrally-multiplexed techniques. At least one channel is required for the thermometry fluorophore, and a second may be required for a temperature-insensitive reference to correct for fluctuations in excitation. While multiplexed quantitative polymerase chain reaction (qPCR) utilizing up to six fluorophore channels has been recently reported [20], the inclusion of a real-time optical thermometry system would still involve a 16% or 33% reduction in throughput, depending on the use of a one- or two-channel system.

To provide accurate thermometry for infrared laser-assisted heating in microdroplet PCR [11–13], we have developed a temperature calibration method that relies on the melting of contact-quenched fluorescently labeled DNA oligomers. An oligomer labeled with a 5' fluorescent reporter is contact-quenched by a 3' quencher on the reverse complement upon hybridization [21–24]. With heating and dissociation of the hybrid pair, the fluorescence of the reporter oligomer is detected and recorded. The melting points of several oligomer pairs are assigned with a traditional qPCR instrument and used to calibrate temperature in the microdroplet with laser heating when this process is repeated at the microscale. This method not only provides a reliable and consistent calibration for microdroplet heating, as demonstrated by proper selection of heating parameters for qPCR, but it is also simple and straightforward to perform. Although we use this method for system calibration, it could be applied to online temperature monitoring during PCR while consuming only a single fluorescence channel.

Because premelting of DNA oligomers prevents modeling the fluorescence melting curve as a conventional (one-term) sigmoid that applies to a two-state system, we have also developed a model based on a three-term sigmoid that allows determination of precise melting temperatures from a fluorescence melting curve using curve fitting even when the premelting fluorescence is quite large. Calibration over a broader temperature range is obtained using a mixture of multiple oligomer pairs. The three-term sigmoid fitting allows for the use of common fluorescent DNA labels, such as fluorescein amidite (FAM), that can induce non-two-state melting behavior [25] as well as the use of high melting temperatures (85 °C for our longest oligomer with 47 base pairs).

## **2. Materials and methods**

### *2.1 Reagents and DNA oligomers*

Three reverse-complement pairs of DNA oligomers were designed for contact-quenching based on the work of Marras et al. [21]. The three sequences, hereafter referred to as Oligo 20, Oligo 27, and Oligo 47, are listed in Table 1. The sequences were labeled with 5'-6-FAM while their reverse complements were each labeled with 3'-Dabsyl, enabling each pair to engage in static-contact quenching when annealed. All oligos were synthesized by the Protein and Nucleic Acid Facility at Stanford University (Stanford, CA). Aqueous stock solutions of

each oligo (100 – 500  $\mu$ M) were prepared and stored in the dark at  $-20^{\circ}\text{C}$ . Because both the diameter of microdroplets generated and oligomer melting temperature depend on buffer conditions, all subsequent oligo solutions were created in PCR master mix at 1X concentration (TaqMan Fast Universal, Life Technologies).

Solutions containing 2  $\mu$ M of each reporter oligo and 10  $\mu$ M of its reverse-complement quencher were prepared. The five-fold excess of quencher both minimizes the influence of unquenched dye on the results and simplifies the determination of melting temperatures, as demonstrated below. Solutions were further diluted to create 40- $\mu$ L samples containing individual reporter-quencher pairs as well as mixtures of all three pairs. In all final solutions, Oligo 20 was prepared at 0.67  $\mu$ M/3.3  $\mu$ M FAM/Dabsyl, Oligo 27 was prepared at 0.50  $\mu$ M/2.5  $\mu$ M FAM/Dabsyl, and Oligo 47 was prepared at 0.83  $\mu$ M/4.2  $\mu$ M FAM/Dabsyl. Solutions containing only the reporter oligo at the same concentrations were also prepared for correction of temperature-quenching of the dye.

**Table 1. DNA Oligomer Sequences**

Name	Sequence (3' to 5')
Oligo 20	TTTTTAAACATATAATACGG
Oligo 27	TTTTCACAGTTACCAGAGGGTCTAT
Oligo 47	CCCTGGGACCCGAGACTCGGCACGGGCCGGAGGTGCGCGACAGCGG

Sequences of three DNA oligomers used for temperature calibration of microdroplet laser heating. Oligo names are derived from the number of bases in each sequence (i.e., Oligo 20 is 20 base-pairs long.)

All 40- $\mu$ L samples were run on an ABI 7300 Real-Time PCR System (Applied Biosystems) in an ABI Prism 96-well Optical Reaction Plate using a dissociation curve protocol. After holding at  $95^{\circ}\text{C}$  for 15 seconds, the samples were annealed by lowering the temperature to  $36^{\circ}\text{C}$  for 1 minute and then they were melted by raising it to  $96^{\circ}\text{C}$  for 15 seconds. The temperature was ramped at  $\pm 1.1^{\circ}\text{C/s}$  for both annealing and melting. Raw fluorescence data was exported from the instrument and analyzed using a three-term sigmoid model, described below, to extract the melting temperatures.

## 2.2 Microdroplet production and imaging

A clear, 35-mm polystyrene Petri dish (Nunc, Thermo Fisher Scientific) was cleaned with methanol and dried with compressed air. A Zerostat gun was used to minimize the surface charge on the dish. 1.5 mL of sterile-filtered embryo tested mineral oil (Sigma) containing 0.4 mL of lecithin / 5 mL mineral oil was pipetted into the dish. The Petri dish was placed on the platform of the imaging microscope described below.

Oligo sample solutions were prepared in the same manner (as above) for macroscale melting. Microdroplets of oligo samples in 1X PCR master mix buffer, approximately 250  $\mu$ m in diameter, were deposited onto the Petri dish under the surface of the mineral oil to prevent evaporation and maintain a high contact angle. Microdroplet deposition was accomplished by injecting sample solution through a capillary via pressure while the capillary was dipped under the mineral oil, as described elsewhere [11–13]. Mineral oil was used because it has a lower density (0.82 – 0.88 g mL $^{-1}$ ) than water and has extremely low water solubility.

Microdroplets were imaged using an inverted fluorescence microscope (TE2000, Nikon Instruments) containing a dual filter-turret and fitted with a 10x Nikon objective. Figure 1 illustrates the system design. The top filter cube is used for fluorescence excitation and emission collection and the bottom filter cube delivers an infrared (IR) beam from a diode laser (FOL 1402PLY-617-1457, Furukawa Electric) of wavelength 1.46  $\mu$ m for heating the microdroplet. A current source (LDX-3620, ILX Lightwave) under computer control varies the laser power for thermal cycling. Band-pass filters are used for fluorescence detection with a 480/40-nm filter for excitation and a 535/50-nm filter for emission. All dichroics and filters were purchased from Chroma (Bellows Falls, VT).

A two-lens telescope and 4-f two-lens configuration based on Thorlabs cage systems are utilized to adjust collimation and couple the laser to the microscope. Defocusing the laser beam at the microdroplets is achieved by translating one lens in the telescope in order to achieve a  $\sim 300$ -nm beam size and obtain a relatively uniform temperature distribution. The laser beam position and size are monitored using a transparent tape coated with a thin layer of erbium upconverting phosphor powder. Brightfield and fluorescence images are acquired with a cooled charge-coupled device (CCD) camera (Retiga EXi, QImaging). For DNA oligomer melting curve studies, the power of the laser was ramped between 0 and 63 mW, stepping up by 0.15 mW and holding for 5 seconds at each step. Fluorescence and brightfield images were taken at 3 and 4 seconds into the hold, respectively. All experiments were conducted at ambient temperature (23 °C).

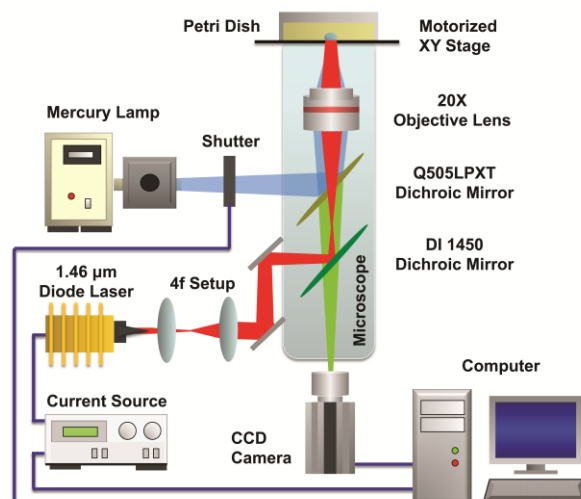


Fig. 1. Instrument schematic for microdroplet heating with an infrared diode laser and imaging of sample fluorescence.

### 2.3 Microdroplet PCR

PCR reaction solutions were prepared by combining 20 μL of TaqMan Fast Universal 2X master mix with 4 μL human male DNA (Applied Biosystems), 2 μL FAM-labeled 18SRNA primer-probe (Hs03928985\_g1 TaqMan Expression Assay, Applied Biosystems), and 14 μL PCR-grade water (Ambion). Microdroplets of the reaction mixture were deposited on a Petri dish coated in mineral oil as described above. No treatment is necessary to prevent adsorption of DNA to the polystyrene surface.

Thermocycling protocol for TaqMan Fast Universal PCR Master Mix was converted to laser power using the melting curve calibration described below. This PCR protocol, for an ABI 7300 instrument, consists of an activation and denaturation step of 30 seconds at 95 °C, followed by 40 cycles of 30 seconds at 60 °C (annealing/extension) and 1 second at 95 °C (denaturation). The data shown below was obtained using laser power settings corresponding to 60 °C and 95 °C, respectively. Additionally, tolerance of the PCR reaction in the microdroplet was explored by testing the reaction at various power settings corresponding to 5 °C steps in the annealing/extension and denaturing temperatures. The results of these reactions were then compared to 25-μL reactions of the same PCR mixture run in a desktop instrument (AB7300, Applied Biosystems).

Droplets were imaged after the first 3 seconds of the annealing phase of each cycle for real-time FAM and brightfield detection, controlled in LabVIEW. The average pixel intensity for each droplet is tracked through 40 cycles of PCR. Fluorescence images are acquired with



a 300-ms acquisition time and brightfield images are acquired with a 5-ms acquisition time to avoid observable fluorescence bleaching effects. The fluorescence illumination source is blocked with an automated shutter between fluorescence measurements.

### 3. Results and discussion

#### 3.1 Macroscale melting analysis of reporter-quencher DNA oligos

Individual contact-quenched hybrid pairs of Oligos 20, 27, and 47 in PCR master mix buffer solutions were analyzed via thermal dissociation to obtain their fluorescence melting curves. Samples of each oligomer pair, as well as a mixture of all three oligomer pairs, were analyzed in replicates of 5. Melting curves were divided by the fluorescence of solutions containing only the reporter-labeled oligos to correct for thermal quenching of the fluorescent dye.

As will be further discussed below, the plots of fluorescence as a function of temperature do not fit well to the simple single-term sigmoid shape expected for two-state bimolecular melting/hybridization of two complementary DNA oligomers [26]. This discrepancy is due to a “premelt” fluorescence contribution that arises from disruption of the static, contact-quenched dimer of the 5'-FAM reporter and 3'-Dabsyl quencher. This premelt fluorescence increases with temperature as the reporter and oligomer achieve greater average distances apart due to “breathing” motions of the hybridized pair [27]. It is important that we include this effect in our model of the fluorescence temperature dependence to obtain accurate results.

To account for this premelt fluorescence, we approximate the system as an equilibrium of three states as shown in Fig. 2: the contact-quenched hybrid pair,  $FQ$ , a premelted pair in which the reporter and quencher are not in static contact,  $FQ^*$ ; and the completely unquenched, melted pair, reporter  $F$  and quencher  $Q$ . The system is described by the equations

$$K_1 = \frac{[F][Q]}{[FQ]} \quad (1)$$

$$K_2 = \frac{[FQ^*]}{[FQ]} \quad (2)$$

$$K_3 = \frac{[F][Q]}{[FQ^*]} \quad (3)$$

where  $K_1$ ,  $K_2$ , and  $K_3$  are temperature-dependent equilibrium constants for each state change and the quantities in square brackets indicate temperature-dependent concentrations in each state.

Note that we are treating  $[FQ^*]$  as a single state although the premelted molecules will actually have a continuum of dye-quencher distances with different levels of fluorescence: some fully-quenched, some fully unquenched with fluorescence similar to the denatured states, and some with partially quenched fluorescence. Treating  $[FQ^*]$  as a single state is valid with the appropriate definition of the concentrations  $[FQ^*]$  and  $[FQ]$ . In particular, we define  $[FQ^*]$  as the combination of the fully unquenched premelt molecules with an appropriate fraction of the partially quenched premelt molecules such that the product of this combined concentration  $[FQ^*]$  times the fully unquenched fluorescence per molecule is equal to the total premelt fluorescence. The remainder of the partially quenched states and the fully quenched states are included in the state  $[FQ]$  to account for all the annealed oligomers. This simplified accounting is similar in principle to the two-state equilibrium of Eq. (1) in which any given oligo is neither annealed nor free, but is annealed for part of the time or denatured for part of the time. This definition of  $[FQ^*]$  and  $[FQ]$  accounts for the total number of premelted molecules (since the population of partially-quenched molecules is split into dark

and unquenched subpopulations) and accounts for the total fluorescence, since we have defined the subpopulations to ensure the total fluorescence is the equal to the actual fluorescence. However, because this definition of  $[FQ^*]$  does not correspond to a conventional molecular state, the associated enthalpy that defines its coordinate in the reaction,  $\Delta H_p$ , is not a true enthalpy but is instead a mathematical construct that assigns the population with a partially-quenched fluorescence brightness to a smaller averaged population with a fluorescence corresponding to an unquenched state.

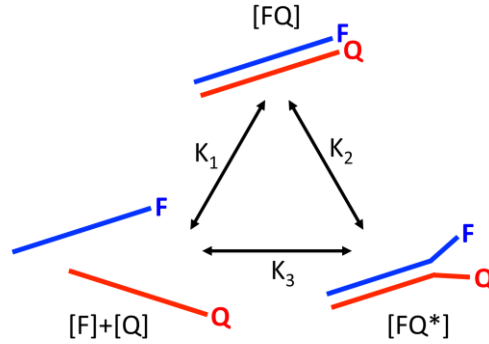


Fig. 2. Three-state equilibrium that describes the melting process of a static-quenched DNA oligomer pair. The premelt fluorescence we observe is accounted for by the existence of an intermediate state  $FQ^*$  in which distance-based fluorescence resonance energy transfer (FRET) quenching is in effect.

It is convenient to introduce a pseudoequilibrium constant,  $\kappa$ , which expresses the ratio of fluorescing states  $[FQ] + [FQ^*]$  to the dark states  $[FQ]$

$$\kappa = \frac{[F] + [FQ^*]}{[FQ]} = \frac{K_1}{[Q]} + K_2. \quad (4)$$

Note that from the rightmost equivalence in Eq. (4),  $\kappa$  has the approximate behavior of a sum of two equilibrium constants, though neither term in the sum is a true equilibrium constant since the first term includes the factor  $[Q]$  and the second term  $K_2$  couples  $[FQ^*]$ , which is not a single molecular state. However, as seen below, this framework provides a good description of our experiments.

We define the fractional concentrations of fluorescent states  $f$  as

$$f = \frac{[F] + [FQ^*]}{[F] + [FQ^*] + [FQ]} = \frac{\kappa}{1 + \kappa} = \frac{1}{1 + 1/\kappa}. \quad (5)$$

where the denominator is the total concentration of dye-labeled oligomers. Solving Eq. (5) for  $\kappa$  gives

$$\kappa = \frac{f}{1 - f}. \quad (6)$$

Because of the way we have defined  $[FQ^*]$  and  $[FQ]$ ,  $f$  is both the fraction of dye-labeled oligomers in equivalent fluorescent states and the average fluorescence from a population of dye-labeled oligomers. Although not shown explicitly, all parameters in Eqs. (4)–(6) are temperature-dependent, and  $f$  describes the fluorescence melting curve normalized from zero to one. When  $[FQ^*]$  is negligible, the  $f$  and  $\kappa$  depend on melted ( $[F]$ ,  $[Q]$ ) and annealed ( $[FQ]$ ) states only, which is the two-state solution of Eq. (1). For the two-state

solution and large excess of  $[Q]$ ,  $f$  takes the form of a sigmoid and  $\kappa$  has Arrhenius behavior (it is a straight line on an Arrhenius plot as described further below).

For our experiments,  $[FQ^*]$  is not negligible, and  $f$  and  $\kappa$  have fluorescence contributions from both melting and premelting. Indeed, plots of the normalized experimental fluorescence melting curves,  $f$ , show strong departures from the sigmoid shape expected for a conventional two-state melting behavior, particularly for the 47-mer oligo, as shown in Fig. 3(a). Similarly, if we make Arrhenius plots of the same data. i.e.,  $\ln(\kappa)$  versus  $1/T$  with  $T$  in Kelvin, we find two distinct regions, as shown in Fig. 3(b). In fact, the two regions are linear, indicating that they demonstrate Arrhenius-like behavior. We expect that the high-temperature Arrhenius-like region, denoted as  $\kappa_m$ , corresponds to melting, which we write as

$$\kappa_m(T) = \kappa_m(T_o) \exp \left[ D_m \left( \frac{1}{T_o} - \frac{1}{T} \right) \right] \xrightarrow{\text{equal for high } T} \frac{K_1}{[Q]} = \frac{[F]}{[FQ]} \quad (7)$$

where the Arrhenius-like behavior is shown explicitly in terms of the Arrhenius plot slope  $D_m$  and the Arrhenius plot amplitude  $\ln[\kappa_m(T_o)]$  at a reference temperature,  $T_o$ . Similarly, the low-temperature Arrhenius-like region  $\kappa_p$  corresponds to premelting with behavior

$$\kappa_p(T) = \kappa_p(T_o) \exp \left[ D_p \left( \frac{1}{T_o} - \frac{1}{T} \right) \right] \xrightarrow{\text{equal for low } T} K_2 = \frac{[FQ^*]}{[FQ]}. \quad (8)$$

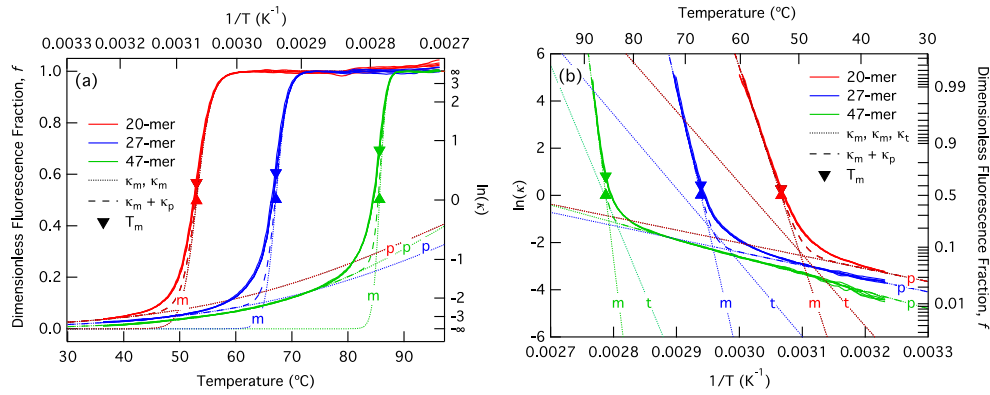


Fig. 3. Experimental data and theoretical fits for fluorescence melting curves. The same data are displayed in two parameterizations: normalized (dimensionless) fluorescence  $f$  versus temperature  $T$  in (a); and as an Arrhenius plot or  $\ln(\kappa)$  versus  $1/T$  in (b). Solid lines show five replicates of experimental data with a different color for each of the three oligos. Dotted lines show the three single-term  $\kappa$  or  $f$  for each oligo, labeled m (melt), p (premelting), or t (transition), appearing as straight lines on the Arrhenius plot (b) and sigmoids in (a). For clarity,  $\kappa_t$  is not displayed in (a). Dashed lines show the two-term calculations  $\kappa_{(2)} = \kappa_m + \kappa_p$ , and  $f_{(2)}$  in (b) and (a), respectively, demonstrating good fits to the experimental data in the high- and low-temperature regions, but poor agreement in the transition region. The three-term calculations  $\kappa_{(3)} = \kappa_m + \kappa_p + \kappa_t$  and  $f_{(3)}$  precisely overlap the data (not shown for clarity; see Fig. 4 for examples). Two points at  $T = T_m$  are shown: upward pointing triangles at  $\kappa_m = 1$  or  $f_m = 1/2$  (which define  $T_m$ ) and downward pointing triangles on  $\kappa_{(3)}$  or  $f_{(3)}$  at the same temperature. For comparison between the parameterizations  $\kappa$  or  $f$  and  $T$  or  $1/T$ , the other parameterizations are shown on the opposing axes (right and top axes). While full experimental data sets are shown in (a), in (b) we only show data values for  $f < 0.995$  to minimize the noise that would obscure part of the linear fits.

We expect strict equality between the left and right parts of Eqs. (7) and (8) only for the high- and low-temperature regions, respectively, because of the complications in the transition region as discussed below. The various pseudoequilibrium constants  $\kappa$  and

associated sigmoid curves,  $f$ , are summarized in Table 2. When  $\kappa$  is the sum of two or three Arrhenius terms, we refer to the resulting shape for  $f$  as a two- or three-term sigmoid, or  $f_{(2)}$  or  $f_{(3)}$  respectively. Although there are other asymmetric sigmoid or logistic functions [28, 29], the ones presented here are based on a physical model for our experiments and perform very well at all temperatures as shown in Figs. 3 and 4.

**Table 2. Pseudoequilibrium Constants  $\kappa$  and Associated Sigmoid Curves  $f$**

$\kappa$ Terms	$f$ Terms	Notes
$\kappa_m$	$f_m$	Melt or two-state term, dominates at high T
$\kappa_p$	$f_p$	Premelt term, dominates at low T
$\kappa_t$	$f_t$	Transition term
$\kappa_{(2)} = \kappa_m + \kappa_p$	$f_{(2)}$	Two term case
$\kappa_{(3)} = \kappa_m + \kappa_p + \kappa_t$	$f_{(3)}$	Three term case

Table of pseudoequilibrium constants  $\kappa$  and associated sigmoid curves  $f$  as calculated from the  $\kappa$  values using Eq. (5). We refer to  $f_{(2)}$  and  $f_{(3)}$  as a two-term sigmoid and three-term sigmoid, respectively.

We would expect  $\kappa_m$  to follow Arrhenius behavior since it describes the proportion of  $[F]$  and  $[FQ]$  in the high-temperature region, and  $\kappa_m$  should follow  $K_1$  in behavior since  $[Q]$  is in excess and its value, compared to the range of  $K_1$ , is relatively constant. The fact the  $\kappa_p$  follows Arrhenius behavior is unanticipated because  $[FQ^*]$  is not a single well-defined state. Converting the high-temperature and low-temperature limiting cases, or  $\kappa \sim \kappa_m$  and  $\kappa \sim \kappa_p$ , respectively, of Fig. 3(b) into fluorescence melting curves  $f_m$  and  $f_p$  using Eq. (5) gives single-term sigmoids showing good agreement with the experimental data in these limits, shown as dotted lines in Fig. 3(a).

Anticipating that  $\kappa$  is a sum of  $\kappa_m$  and  $\kappa_p$  based on Eq. (4), we plot  $\kappa_{(2)} = \kappa_m + \kappa_p$  and the associated  $f_{(2)}$  as the dashed lines in Figs. 3(b) and 3(a), respectively. While both curves agree well with experiment in the high- and low-temperature regions, the transition regions do not have the proper shape. To better fit the entire data set, a third transition Arrhenius-behavior term,  $\kappa_t$ , is added to the  $\kappa_m + \kappa_p$  sum to better approximate the behavior of the transition region, giving a three-term expression for  $\kappa_{(3)} = \kappa_m + \kappa_p + \kappa_t$  (Table 2). The physical behavior of this transition region is likely complex and beyond the scope of this paper. However, the  $\kappa_t$  term is useful for fitting the data and obtaining a reproducible melting temperature. The result from the three-term fit exactly overlaps with the data for both the Arrhenius plot and the fluorescence melting plot.

For fitting experimental data in which we are interested in extracting the melting temperature,  $T_m$ , it is useful to express  $\kappa$  and  $f$  in terms of this parameter. Thus, we will use  $T_m$  as the reference temperature  $T_o$  in Eqs. (7) and (8). The experimental definition of the melting point is complicated because: (a) the conventional melting point is only properly defined for a two-state model for which exactly half of the oligos are denatured, and (b) the details of the equilibria in the transition region are not well defined. Note that the high-temperature region is expected to correspond to the two-state conventional melting process as shown in Eq. (7). Indeed, the slopes of these high-temperature lines agree with calculated enthalpies to within 10-15 percent, as discussed below with respect to Table 3. Using this information, we define the melting point for these experiments as an “extrapolated two-state” melting temperature or the point at which  $\kappa_m$  would yield  $[F] = [FQ]$  in Eq. (7) or

$$\kappa_m(T_m) = 1. \quad (9)$$

Since the high-temperature limit  $\kappa_m$  corresponds to the two-state system, the melting temperature defined by Eq. (9) would presumably be the actual melting temperature if the premelting were negligible. Note from Fig. 3(a) that this melting temperature is where the two-state or high-temperature sigmoid  $f_m = 1/2$ . This definition for  $T_m$  circumvents the influence of the premelt and transition regions on the melting point definition and links the melting temperature to the conventional two-state model. Using Eqs. (5), (7), (8), and (9) and  $\kappa_{(3)}$  from Table 2 produces an expression for the fluorescence melting curve of

$$A + Bf_{(3)} = A + \frac{B}{1 + \frac{e^{D_m\left(\frac{1}{T_m} - \frac{1}{T}\right)} + \kappa_p(T_m)e^{D_p\left(\frac{1}{T_m} - \frac{1}{T}\right)} + \kappa_t(T_m)e^{D_t\left(\frac{1}{T_m} - \frac{1}{T}\right)}}}{1}} \quad (10)$$

where  $T_m$  is used as the reference temperature and an Arrhenius equation similar to Eq. (7) is used for  $\kappa_t$ . To allow comparison with experiment, we use  $A$  as the initial background fluorescence and  $B$  as the maximum increase in fluorescence during the melting process.

**Table 3. Three-Term  $\kappa$  Fit Parameters**

	<b>Oligo 20</b>	<b>Oligo 27</b>	<b>Oligo 47</b>
$T_m$ (°C)	53.0	67.1	85.6
$D_m$ or $\sim\Delta H_m/R$ ( $10^3$ K)	81.8	118.1	216
$\Delta H_m/R$ (calc, $10^3$ K)	74	102	201
$\kappa_p(T_m)$	0.09	0.13	0.35
$\kappa_t(T_m)$	0.23	0.40	0.89
$D_p$ ( $10^3$ K)	5	6	7.3
$D_t$ ( $10^3$ K)	30	32	64

Fit parameters from application of the three-term  $\kappa$  model to individual oligomer data. Melting enthalpies of the oligomers, as calculated via nearest-neighbor interactions, are included in the third row for comparison purposes. These same values are used for all experimental fits in this paper, i.e., Figs. 3, 4, 5, and 6.

Note that there are eight fitting parameters in Eq. (10): the scaling factors  $A$  and  $B$ ; the three slope constants  $D_m$ ,  $D_p$ ,  $D_t$ ; the two pre-exponential factors  $\kappa_p(T_m)$  and  $\kappa_t(T_m)$ ; and the melting temperature,  $T_m$ . The sensitivity of the melting curve may be optimized by increasing the melting enthalpy, thus increasing the slope constant  $D_m$ , and minimizing pre-melt behavior so that more fluorescence signal is devoted to the main ‘melt’ slope. We determined the slope constants and pre-exponential factors from global fits to the five-replicate single-oligo data sets using the graphing analysis program Igor Pro, in which these values were linked to a single value for all five data sets while  $A$ ,  $B$ , and  $T_m$  were allowed to change for each curve. Although the melting temperature for all five curves in a data set should, in principle, be the same, we found improved results by letting each fit to a different value for  $T_m$ . This led to only  $\sim 0.1$  °C variation between curves within a set. The results from these fits are shown in Figs. 4(a)–4(c), and the fit parameters are summarized in Table 3. The residuals at the top of each figure (i.e., data minus fit) show good agreement between experiment and fit. In particular, the residual variations are primarily random noise in nature. On the other hand, fitting of the two-term versions of the model using  $f_{(2)}$  instead of  $f_{(3)}$  do not agree with data nearly as well, as shown in Figs. 4(d)–4(f). These fits produce residuals with pronounced oscillations for the 27-mer and 47-mer, demonstrating a poor agreement between data and fit. Because of the low melting temperature of the 20-mer, the  $f_{(2)}$  fits perform reasonably well.

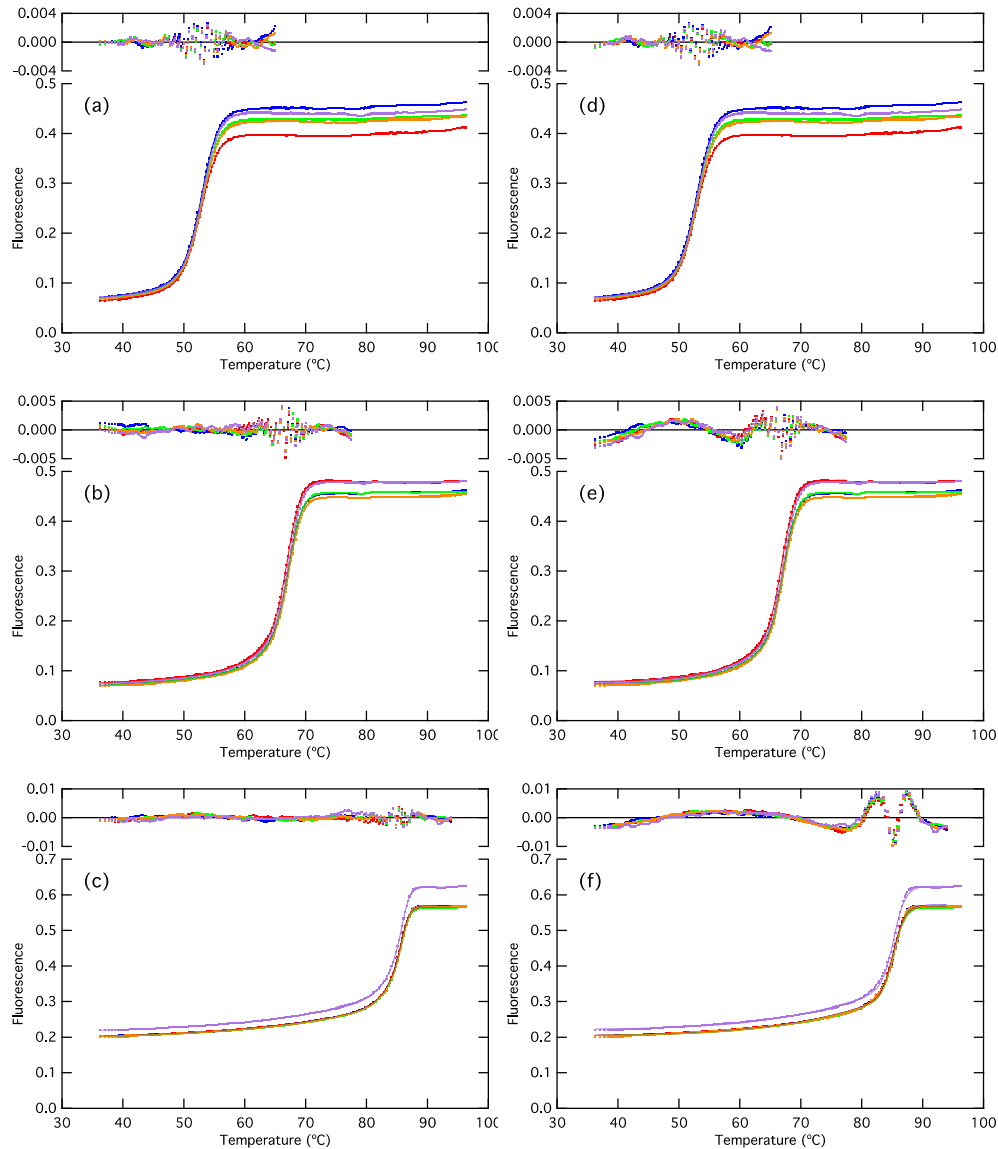


Fig. 4. Fitting of three-term ( $f_3$ , a-c) and two-term ( $f_2$ , d-f) versions of the model to fluorescence melting curves of the 20-mer (a, d), 27-mer (b, e), and 47-mer (c, f) oligomer pairs. The  $f_2$  fit experiences significant deviation from the data in the premelt and melting regions for the 27- and 47-mer data. This deviation is largely absent when the  $f_3$  fit is applied. To minimize systematic effects from fluctuations in the saturated region ( $f \sim 1$ ), fits were performed only up to a maximum temperature given by  $f_m = 0.995$  plus 5 degrees. The same experimental data has been presented in Fig. 3 as  $f$  and  $\kappa$  calculated using the  $A$  and  $B$  determined by the  $f_3$  fits.

We obtain physical parameters that are in agreement with expected values. Since  $[Q]$  is approximately constant, then the high temperature limit  $\kappa_m$  is equal to the two-state equilibrium constant divided by a constant  $[Q]$  which primarily affects the intercept, not the slope of Eq. (7). Thus the slope  $D_m$  should closely approximate  $\Delta H_m/R$ , where  $\Delta H_m$  is the enthalpy of transition of the traditional two-state model, which may be approximately calculated using the nearest-neighbor method [30] for the known oligomer sequences. The experimental values for  $D_m$  from the fits (Table 3, row 2) are in reasonable agreement with

the nearest-neighbor values  $\Delta H_m/R$ , (Table 3, row 3). Additionally, the quantity  $D_p$  for Oligos 20 and 27 (Table 3, row 4), which represents the ratio of the premelting enthalpy of equilibrium  $K_2$  to the two-state melting enthalpy, is in reasonable agreement for the values that are obtained for poly(dA)•poly(dT) tracts [31]. Oligos 20 and 27 contain 5-mer dA•dT tracts next to the quencher/reporter. Oligo 47 lacks such a tract.

For a given oligomer, a rough estimate of the contribution of premelt to a measurement is the point where the premelt and melt terms are equal, or  $f_m = f_p$ . For  $T$  below this point *premelting* becomes more important, while above this point *melting* becomes more important. For our oligos, we find  $f_m = f_p = 0.07, 0.11$ , and  $0.25$  for the 20-mer, 27-mer, and 27-mer, respectively [see also Fig. 3(a)].

### 3.2 Temperature calibration of infrared heating laser

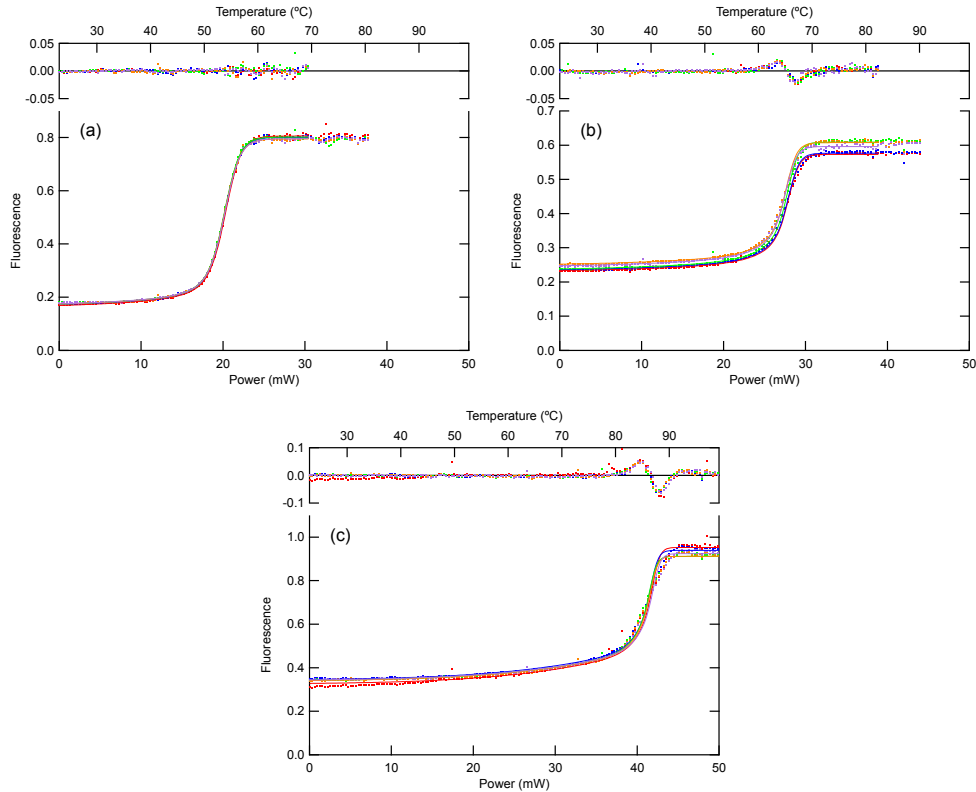


Fig. 5. Fluorescent melting curves of Oligos 20(a), 27(b), and 47(c) in a microdroplet heated by an infrared laser. Single-oligo premelt model fit is applied using parameters of Table 3 and similar results are obtained as from application to the macroscale melting curves. Note that discrepancies in fit become larger with the oligomer length. The temperature axis at the top of each graph is calculated from the calibration curve in Fig. 7.

Microdroplets containing the same solutions of Oligos 20, 27, and 47 and a mixture of all three were analyzed via thermal dissociation to obtain their fluorescence melting curves using laser-assisted heating. As with the dissociation curves obtained from the qPCR instrument described above, the curves were corrected for thermal quenching. Figure 5 shows the corrected microdroplet dissociation curves fitted using the same model described above and the parameters from Table 3 for melting curves obtained via macroscale melting. Since our measured parameter is laser power rather than temperature, we replace the temperature  $T$  in Eq. (10) with

$$T = T_a + \alpha P \quad (11)$$

where  $T_a$  is the ambient temperature,  $P$  is the laser power, and  $\alpha$  is the proportionality between laser power and droplet temperature. For the macroscale fits [Figs. 4 and 6(a)], the independent variable is  $T$ , and  $T_m$  is a fitting parameter. For the microdroplet fits [Figs. 5 and 6(b)],  $P$  is the independent variable,  $T_m$  is fixed to the value in Table 3,  $T_a$  is set to 23 C, and  $\alpha$  is a fitting parameter. From Fig. 5, we see that there is some increasing discrepancy between data and fit with increasing oligomer length, which may be due to deformation of droplet shape with increasing temperature. This is reflected in the increasing variance of the melting power with oligo length (0.06 mW for the 20-mer oligo versus 0.2 mW for the 47-mer oligo). However, the fit is sufficient for our purpose of calibrating the droplet temperature.

For a solution containing a mixture of all three quenched pairs, the same model may be applied by simply extending Eq. (10) to be a sum of four terms

$$A + f_{20}B_{20} + f_{27}B_{27} + f_{47}B_{47}. \quad (12)$$

where  $f_i$  and  $B_i$  are the fractional fluorescence and maximum scaling factor for each oligo, respectively. Figures 6(a) and 6(b) show fluorescent melting curves of both macroscale and microdroplet samples that contained all three oligomer pairs fitted to this three-oligo version of the model and the parameters of Table 3. There is some non-random structure in the residuals. However, the root-mean-square (rms) values of the residuals for the macro droplets [Fig. 6(a)] are quite small (0.001, or 0.2% of the maximum fluorescence levels).

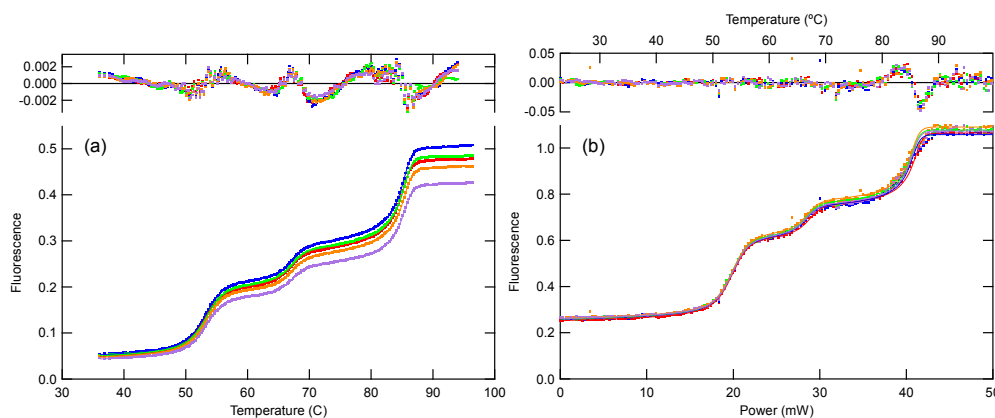


Fig. 6. Fluorescent melting curves of samples containing all three oligo quenched pairs, both at the macroscale (a) and in microdroplets (b). Three-oligo premelt model fit is applied. The temperature axis in (b) is calculated from the calibration curve in Fig. 7.

A calibration curve for microdroplet temperature under laser-assisted heating was constructed using the macroscale melting temperatures and the laser power on the microdroplet obtained from the samples containing mixtures of all three oligo pairs [Fig. 6(b)]. The fits give a simple linear relationship as shown in Fig. 7. This curve was used to obtain appropriate laser power settings for conducting qPCR.

### 3.2 Temperature-calibrated microdroplet PCR

Using the calibration curve obtained for microdroplet temperature under laser-assisted heating, a PCR protocol based on laser power was obtained in place of a conventional temperature-based protocol. This protocol was used to conduct qPCR of the 18S RNA gene (TaqMan Hs03928985\_g1) in human male DNA at a concentration of 0.4 ng/ $\mu$ L or approximately 2 copies of the genome per 250- $\mu$ m microdroplet. Figure 8 shows both microdroplet qPCR amplification curves as well as those for replicate reaction samples run in



a conventional real-time qPCR instrument (ABI 7300, Applied Biosystems). A range of annealing and extension temperatures was tested to determine the tolerance of this qPCR reaction in both reaction environments.

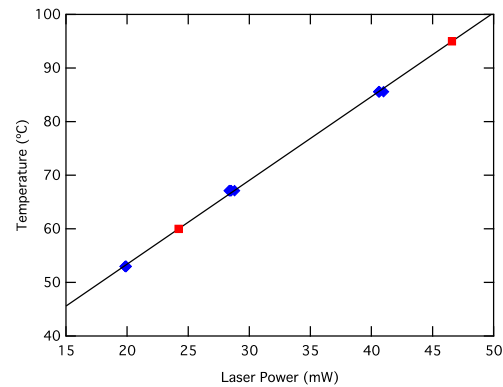


Fig. 7. Calibration curve for heating a microdroplet with an infrared laser. A linear relationship (black) is obtained when oligomer melting laser voltages are plotted against oligomer melting temperatures (blue). The regression line is interpolated to obtain a laser power corresponding to 60 °C and extrapolated to obtain a laser power corresponding to 95 °C (red).

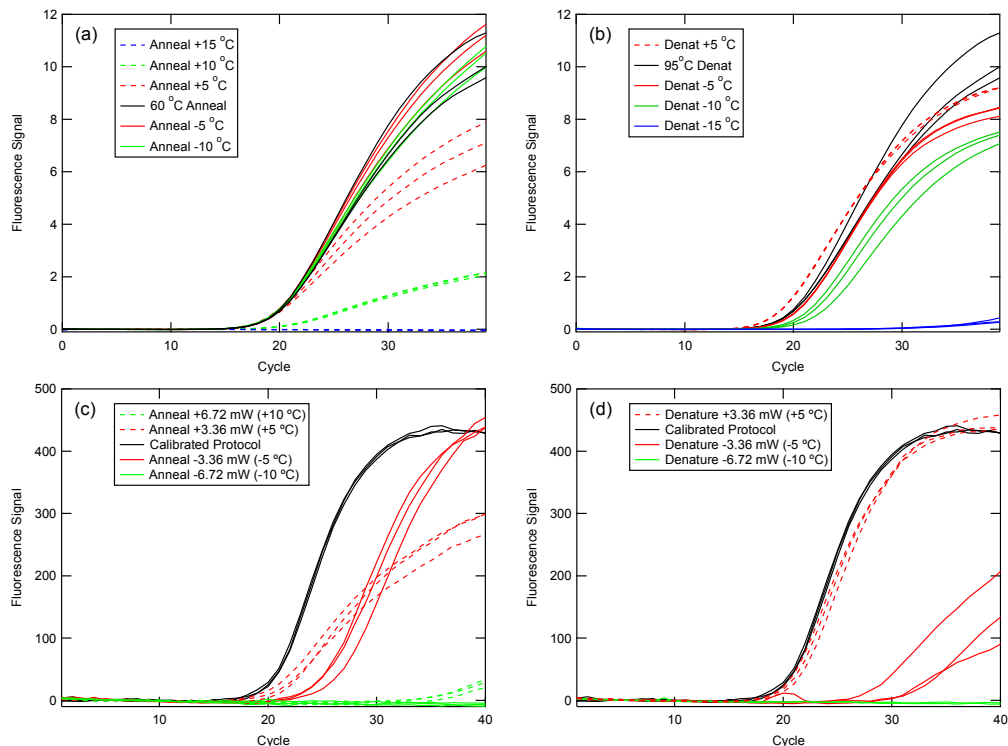


Fig. 8. Real-time qPCR amplification curves for macroscale (a, b) and microdroplet instrument (c, d) reactions. Effective ranges for the microdroplet around the calibration are explored and compared to the range of a qPCR instrument. The calibration curve for this experiment gives approximately a 1 °C / 0.66 mW slope.

Calibration of laser heating gave effective qPCR without any additional adjustment. Exploration of the surrounding annealing and denaturation temperatures in the macroscale instrument by 5 °C increments reveals that reaction mixture used in this work tolerates a wide

range of temperatures [Figs. 8(a) and 8(b)]. The microdroplet reaction appears to exhibit a lower tolerance in the microdroplet [Figs. 8(c) and 8(d)]. It is not clear whether the higher sensitivity to reaction temperatures for the microdroplet is due to the sample size, sample environment, or the temperature ramp rate, which is approximately 100 times faster for the microdroplets. It should be noted though that the standard calibration appears to give the most efficient (earliest amplification) protocol for a microdroplet among the tested values. Therefore, we believe that the calibration serves as an effective method for establishing an effective PCR protocol. Additionally, it has consistently produced such protocols even after alignment changes in the infrared laser.

#### **4. Conclusions**

We have developed a novel method for the calibration of heating microscale volumes via the fluorescent melting curves of static-quenched oligomers. This method allows for effective qPCR in microdroplets heated with an infrared laser and minimizes complications due to optical changes, including drift in infrared laser alignment and variation in the size of the absorbing microdroplet. The use of labeled oligomers is more expensive than common dyes such as rhodamine (roughly by a factor of 100), but because the measurements are performed in droplets with a volume of roughly 10 nL and the calibration remains valid for the duration of an assay, the calibration cost is very low (less than a penny for labeled oligos for a five-droplet calibration run). In conjunction with this method, we have also developed a model for the melting of quenched labeled oligomers that follow non-two-state melting behavior. This three-term sigmoid model extracts the two-state melting temperature from the melting curves, overcoming limitations from pre-melting to quantification of fluorescence melting curves. We believe that this method may be extended to other fluorescent studies of DNA hybridization, including hairpin folding [24, 32], as well as the array of other dye-quencher pairings that are available [21, 22]. Implementation of calibration in the same droplet undergoing PCR during the initial ramp to heat activation of the polymerase may also control for variance in droplet size and shape by tuning the protocol on a per-droplet basis.

#### **Acknowledgments**

This research was supported by funds from the DOD Breast Cancer Research Program (grant number W81XWH-12-1-0076; the U.S. Army Medical Research Acquisition Activity, 820 Chandler Street, Fort Detrick MD 21702-5014 is the awarding and administering acquisition office) and internal research and development funds from SRI International. The content of this paper does not necessarily reflect the position or the policy of the government, and no official endorsement should be inferred. We acknowledge experimental contributions from Bio Guo and Chia-Pin Pan.